UNIVERSITÀ DEGLI STUDI DI PADOVA

Dipartimento di Fisica e Astronomia "Galileo Galilei"

Master Degree in PHYSICS

Final Dissertation

Magnetohydrodynamic stability analysis of the pedestals of ASDEX Upgrade plasmas

Thesis supervisor

Dr. Lidia Piron *Università degli Studi di Padova*

Thesis co-supervisors

Dr. Clemente Angioni *IPP Garching*

Dr. Michael G. Dunne *IPP Garching*

Dr. Teobaldo Luda di Cortemiglia *IPP Garching*

Candidate

Michela Salinaro

Academic year 2022/2023

Contents

1 Introduction **1**
1.1 The path to a sustainable future . . . 1
1.1.1 Plasma: the fourth state of matter . . . 3
1.1.2 Brief overview of Nuclear Fusion . . . 4
1.1.3 Magnetic Confinement Fusion: an approach to generate fusion power . . . 7
1.1.4 An experimental machine to harness fusion: the tokamak . . . 8
1.1.5 ASDEX Upgrade: a divertor tokamak . . . 12

2 Theoretical overview **15**
2.1 Pedestal: H-mode effect . . . 15
2.1.1 Edge localized modes . . . 16
2.1.2 Ideal magnetohydrodynamics . . . 17
2.1.3 Stationary ideal MHD equilibrium . . . 19
2.1.4 Linear MHD stability . . . 21

3 Methods, tools and workflow **23**
3.1 Diagnostics . . . 23
3.1.1 Measurements of n_e and T_e . . . 24
3.1.2 Measurements of n_e . . . 24
3.1.3 Measurements of T_e . . . 25
3.1.4 Measurements of T, n and rotation of light nuclei . . . 25
3.2 Profile fitting tools . . . 26
3.2.1 Integrated Data Analysis . . . 26
3.2.2 AUGPED . . . 26
3.3 Equilibrium and stability . . . 29
3.4 Workflow . . . 30

4 Stability analysis **33**
4.1 Selection of the time interval . . . 33
4.2 Role of isotope mass . . . 35
4.3 Stability diagrams . . . 36
4.4 Deuterium plasma . . . 38
4.4.1 Discussion on D plasma . . . 45
4.5 Helium plasma . . . 45
4.5.1 Discussion on He plasma . . . 51

5 Conclusions **53**

List of acronyms

AUG	ASDEX (Axially Symmetric divertor Experiment) Upgrade
AUGPED	AUG Pedestal
CXRS	Charge Exchange Recombination Spectroscopy
DEMO	DEMOnstration Power Station
ECE	Electron Cyclotron Emission
ECRH	Electron Cyclotron Resonance Heating
ELM	Edge Localised Mode
ETB	Edge Transport Barrier
GS	Grad-Shafranov
HELENA	Hermite ELements Equilibrium solver for Normal-mode Analysis
HFS	High Field Side
H-Mode	High Confinement Mode
ICRH	Ion Cyclotron Resonance Heating
IDA	Integrated Data Analysis
IPP	Max Planck Institute for Plasma Physics
ITER	International Thermonuclear Experimental Reactor
JET	Joint European Torus
LCFS	Last Closed Flux Surface
LH	Lower Hybrid Resonance Heating
LIB	LIthium Beam
L-Mode	Low Confinement Mode
MHD	Magnetohydrodynamics
NBI	Neutron Beam Injection

PBM	Peeling-Balooning Modes
PFC	Plasma-Facing Component
SOL	Scrape Off Layer
TS	Thomson Scattering

Abstract

The high confinement mode (H-mode) dramatically improves the confinement properties of present tokamak plasmas and is therefore the scenario envisioned for future fusion reactors.
The main characteristic of this scenario is the formation of a pedestal, a zone of steep temperature and density gradients, at the edge of the plasma, by means of a transport barrier. The height of the pedestal is limited by the onset of edge localised modes (ELMs), quasi-periodic explosive instabilities at the plasma edge which expel particles and energy on millisecond time-scales.

While ELMs in present day machines pose no danger, when scaled to a fusion reactor device they are predicted to cause significant damage to the machine components. As such, the understanding and exploitation of alternative regimes with high confinement, but without ELMs, is of significant interest. The onset of an ELM can be described by magnetohydrodynamic (MHD) stability codes.

The aim and project of the current thesis carried out at Max-Planck-Institut für Plasmaphysik (IPP) in Garching (Germany), involves the automation of a workflow which runs codes to test the pedestal MHD stability, such as MISHKA, starting from a standardised set of experimental information. In addition, the HELENA code is employed as a high resolution equilibrium solver through the calculation of the Grad-Shafranov equation for a toroidal axisymmetric plasma.

Once the workflow is implemented, it is applied to a database of experimental data from the ASDEX Upgrade tokamak to study the properties of the pedestal through stability diagrams. It is particularly important to provide an estimate of the distance to the MHD stability boundary in the various ELM-free regimes to understand how robust these regimes are and the margin a given regime has before a large ELM is triggered.

Various deuterium and helium plasma discharges are studied in this regard.

Chapter 1

Introduction

The first chapter introduces the problem of global energy consumption and why it is necessary to explore a possible clean energy solution through nuclear fusion. Afterwards, the plasma, the principles of thermonuclear fusion and magnetic confinement are briefly analysed [1], [2], in particular that of the tokamak [3], specifically describing ASDEX Upgrade [41].

1.1 The path to a sustainable future

Energy resources are essential in the pursuit of humanity's progress. Every economic projection indicates a continuous growth in energy needs. However, relying on the fossil fuels that shaped the civilization of the 19th and 20th centuries comes at a steep price of greenhouse gas emissions and pollution. This rise is mainly summarized in two primary factors:

- an increase in the world's population, predicted to rise to around 10 billion in 2050, with the consequence that industrialization accelerates in developing countries;
- an increase in the energy requirements of developing countries.

The graph 1.1 analyses the global energy consumption, in TWh, as a function of the last approximately 200 years, for each type of energy source.

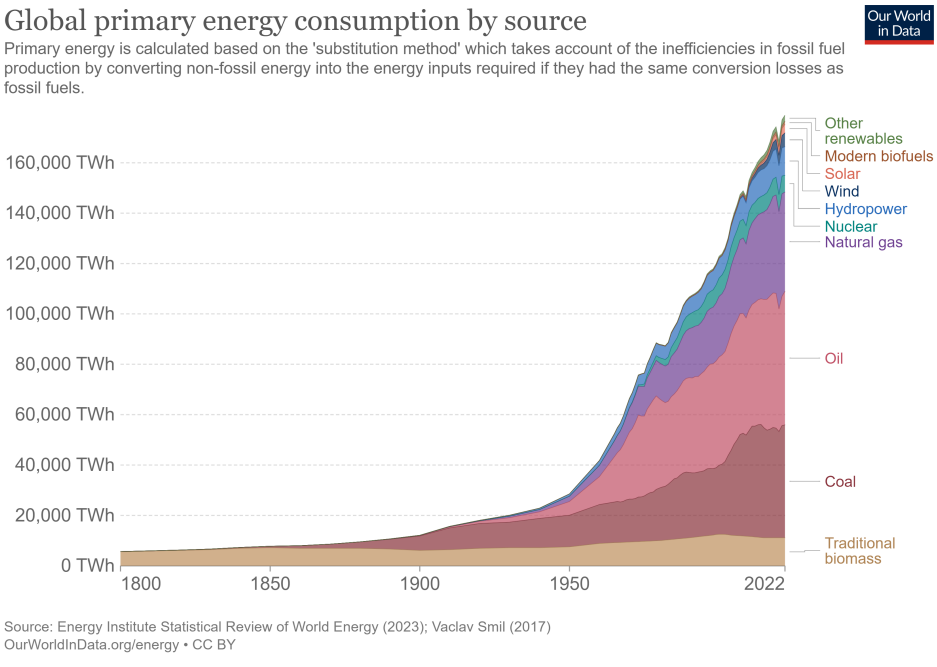

Figure 1.1: Global primary energy consumption (TWh) divided by source, data available until 2022 [42].

The increase in the use of energy sources from the second half of the 19th century due to the technological revolution is clear. The global energy consumption has maintained a nearly consistent upward trajectory, marked by a steep increase over the past five decades. A temporary decrease in 2020 can be attributed to the global Covid-19 pandemic, but the rising trend resumed after a short time. What is also clear is that, the largest amount of energy is derived from oil; coal, gas and non-fossil fuel power sources.

The extensive use of fossil fuels has a substantial impact on the emission of carbon dioxide (CO_2), which serves as the foremost catalyst for worldwide climate change. As a global issue, climate change requires countries around the world to work together. In 2015, in Paris, world leaders agreed on ambitious new targets in the fight against climate change. One of the long-term goals is to keep the global average temperature increase well below 2°C above pre-industrial levels and to continue efforts to limit it to 1.5°C [9]. In figure 1.2, mitigation curves, which represent the possible scenarios through the years, are shown. The sooner we start limiting CO_2 emissions, the sooner we will be able to mitigate the impact of climate change.

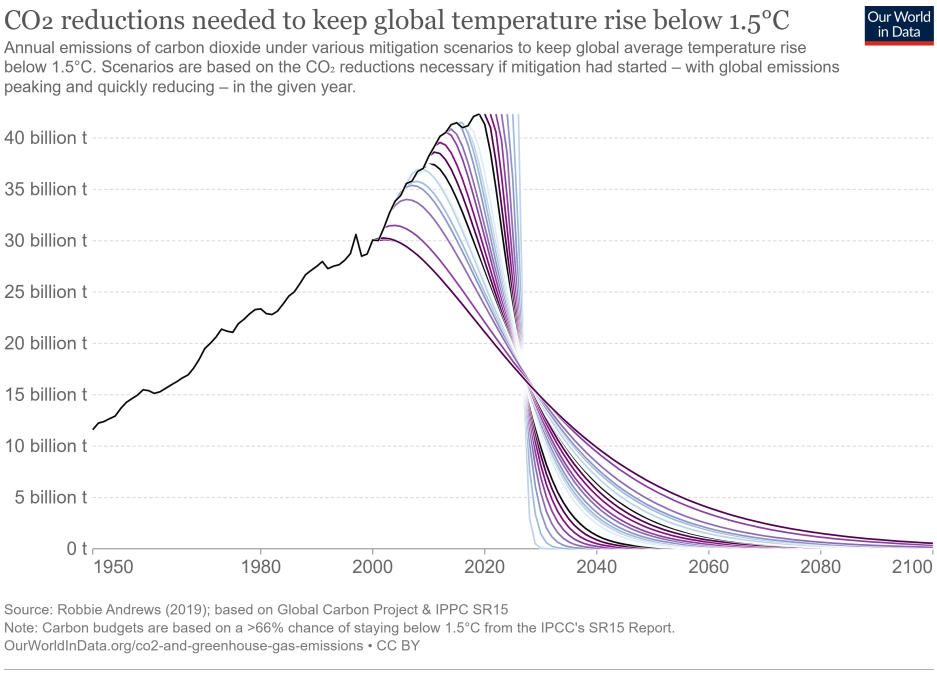

Figure 1.2: CO_2 emissions mitigation curves in order to keep global temperature rise below 1.5°C [43].

The depletion of fossil fuels and the challenge of integrating renewable energy sources into centralized energy production to serve densely populated regions or nations necessitate the emergence of new energy sources. This means that the upcoming decades hold immense significance in setting the course for minimizing the release of greenhouse gases and steering the world towards a more sustainable future. One of the most relevant issues for scientific research concerns the development of new, large-scale, sustainable and carbon-free energy sources, to avoid the worst effects of climate change. These innovative energy forms must not only align with economic prerequisites, but also consider factors like environmental impact, operational safety, resource accessibility, and reliability. Fusion machines avoid the added infrastructure that fossil or nuclear plants require.

In this framework, fusion energy comprehensively fulfils all these criteria and has emerged as a promising and critical solution for the world energy issue. The potential is to revolutionize the world's energy landscape and address some of the most pressing challenges facing humanity in the 21st century. Nuclear fusion offers a safer, cleaner and virtually limitless source of energy and could generate four times more energy per kilogram of fuel than fission (used in nuclear power plants) and nearly four million times more energy than burning oil or coal.

1.1.1 Plasma: the fourth state of matter

Plasma, also defined as fourth state of matter, is a type of *ionised* gas in which at least one of an atom's electrons has been liberated, leaving a positively charged nucleus known as an ion. Normally, plasma can only be found in vacuum. If not, air would cool the plasma, allowing the ions and electrons to join once more to form regular neutral atoms. The Aurora Borealis, fluorescent lights, lightning strikes, are just a few examples of plasmas that we can have on Earth.

The Saha equation indicates the degree of ionization to be expected in a gas in thermal equilibrium:

$$\frac{n_i}{n_n + n_i} \approx \frac{n_i}{n_n} \approx 2.4 \times 10^{21} \frac{T^{3/2}}{n_i} e^{U_i/k_B T} \tag{1.1}$$

where n_i is the density of ionized atoms (number/m^3), n_n the density of neutral atoms, T the gas temperature (K), k_B the Boltzmann constant and U_i the ionization energy of the gas (energy required to remove the outermost electron from an atom). If we take ordinary parameters, such as $n_n \approx 3 \times 10^{25}$ m^{-3}, $T_{room} \approx 300$ K and $U_i \approx 14.5$ eV, we would get a value $n_i/n_n \approx 10^{-122}$.

As the temperature is raises, the degree of ionization remains low until the ionisation energy is only a few times k_BT. Afterwards, the fraction of the two densities rises abruptly, and the gas is found to be in a plasma state. Further increase in temperature makes the density of neutral atoms less than the ionized ones and the plasma eventually becomes fully ionised. This is the reason why plasma exists in astronomical bodies with temperatures of millions of degrees, but not on Earth.
The exponential factor in Saha equation, expresses the fact that the number of fast atoms falls exponentially with U_i/k_BT. Once an atom is ionized, it remains charged until it meets an electron; it then very likely recombines with the electron to become neutral again. The recombination rate clearly depends on the density of electrons, which we can take as equal to n_i.

Any ionized gas cannot be called a plasma, since there is always some small degree of ionization in any gas. A more precise definition is that a *plasma is a quasi neutral gas of charged and neutral particles which exhibits collective behaviour* [2].

Collective behaviour means that the motion depends not only on local conditions, but on the state of the plasma in remote regions as well. Because of collective behaviour, a plasma does not tend to conform to external influences, it often behaves as if it had a mind of its own.

An ideal plasma must satisfy the following 3 conditions:

1. bulk interactions: the Debye length[1] is much smaller than the physical size of the plasma ($\lambda_D \ll$ L). The interactions in the bulk of the plasma are more important than those at its edges, here boundary effects could take place. Satisfying this criterion consists in satisfying the quasi-neutrality one.

2. plasma approximation: it applies when the plasma parameter, representing the number of charge carriers within the Debye sphere, is much higher than unity ($N_D \gg 1$). It can be readily shown that this criterion is equivalent to smallness of the ratio of the plasma electrostatic and thermal energy densities. Plasmas satisfying this criterion are considered as weakly coupled.

3. collisionlessness: the electron plasma frequency (measuring plasma oscillations of the electrons) is much larger than the electron–neutral collision frequency. When this condition is valid, electrostatic interactions dominate over the processes of ordinary gas kinetics. Plasmas satisfying this criterion are considered as collisionless.

[1] In plasmas, the Debye length:

$$\lambda_D = \left(\frac{\epsilon_0 k_B T_e}{n e^2} \right)^{1/2} \tag{1.2}$$

is an important parameter, which measures the charge carrier's electrostatic effect and how far its electrostatic effect persists. With each Debye length, the charges are increasingly electrically screened and the electric potential decreases in magnitude by 1/e. A Debye sphere is a volume whose radius is the Debye length.

To sum up, plasmas can be characterized by the two parameters n and $k_B T_e$. Plasma applications cover an extremely wide range of these two: n varies over 28 orders of magnitude, from 10^6 to 10^{34} m^{-3} and $k_B T_e$ can vary over seven orders from 0.1 to 10^6 eV.
The earliest work with plasmas was that of Langmuir, Tonks and their collaborators in the 1920s. This research was inspired by the need to develop vacuum tubes that could carry large currents and therefore had to be filled with ionized gases.
Plasmas are now studied by the vast academic field of plasma science or plasma physics, including several sub-disciplines such as artificially produced plasma for fusion energy research.

1.1.2 Brief overview of Nuclear Fusion

The energy produced by the Sun results from a process known as nuclear fusion, where p-p chain is dominant fusion reaction. While replicating the exact solar process is unattainable on Earth, the concept of nuclear fusion, which could generate immense energy, has been a human aspiration since the early 20th century. There are several significant challenges that make replicating the Sun's fusion process on our planet extremely difficult. These challenges mainly include the temperature and pressure, the confinement of plasma, the energy input vs. energy output and material and engineering problems. Fusion occurring in the Sun is a slow process, on Earth we need faster reactions.

As opposed to nuclear fission[2], nuclear fusion entails the fusion of two lightweight nuclei, resulting in the creation of a denser nucleus, accompanied by the emission of energy through the kinetic energy of the nucleus as well as other particles like neutrons and photons generated during the process.
In particular, as light nuclei, we consider hydrogen, also called protium ($^1_1$H or simply H) and its isotopes, deuterium ($^2_1$H or simply D) and tritium ($^3_1$H or simply T)) (figure 1.3).

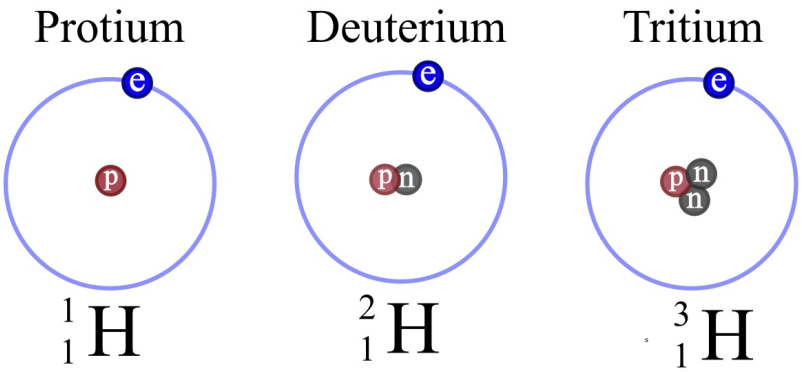

Figure 1.3: Isotopes of hydrogen [44].

The disparity in binding energy between initial reactants and resultant products corresponds to an energy release. This binding energy mirrors the mass discrepancy between the nucleus and its individual constituents, as defined by the formula $E = mc^2$.

In figure 1.4, the binding energy divided by the number of nucleons, which are protons and neutrons, in the nucleus of all the periodic table elements, is plotted as a function of the mass number (A) of the elements. The plot displays that the binding energy per nucleon increases at first sharply with A and is largest for nuclei with mass number around 60. Afterwards, the binding energy per nucleon slowly decreases down to mass numbers 240–250, the uranium isotopes. Nuclei of elements heavier than iron, can in principle yield energy by nuclear fission, while elements lighter than iron can do this in principle by nuclear fusion. Since an increase in binding energy corresponds to energy production, it is apparent that fusion reactions take place in the left part of the plot, involving light nuclei, whereas fission reactions take place in the right part of the graph.

[2]Nuclear fission is a nuclear reaction in which the atomic nucleus of a heavy chemical element decays into nuclei of atoms with lower atomic numbers, lower total combined mass, emitting a large amount of energy and radioactivity.

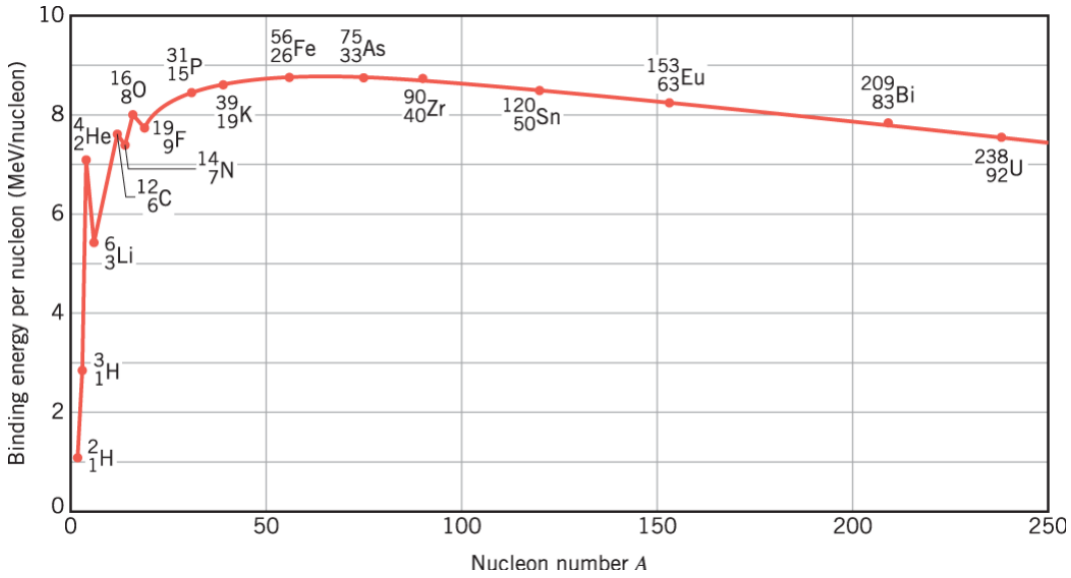

Figure 1.4: Binding energy per nucleon plotted as a function of the number of nucleons.

Fusion is often called "the ultimate energy source" for two primary reasons: firstly, because the fusion of light elements yields the harmless byproduct helium, and secondly, because the foundational fuel for fusion is the hydrogen isotope deuterium, which can be easily sourced from water and is abundantly available to all nations, it will be explained shortly.

In nuclear or subatomic particle physics, it is necessary to mention the cross section, which is the probability that a given atomic nucleus or subatomic particle will exhibit a specific reaction, that could be absorption, scattering, or fission, in relation to a particular species of incident particle. Cross section is expressed in terms of an area, its unit of measurement is the barn (b): 1 b $= 10^{-28}\ m^2$. In nuclear fusion, the reaction cross section measures the probability of a fusion reaction as a function of the relative velocity of the two reactant nuclei.

Considering the cross section dependence on velocity, if the reactants have a distribution of velocities, then it is useful to perform an average over the distributions of the product of cross section and velocity. This average is called the Reactivity, denoted as $\langle \sigma \mathrm{v} \rangle$. In figure 1.5 the Reactivity in function of the temperature for different reactions is plotted.

The main nuclear fusion reactions with the largest cross sections are listed below:

1. $D + T \longrightarrow {}^{4}_{2}\mathrm{He} + n + 17.6\ MeV$
2. $D + D \longrightarrow T + H + 4.032\ MeV$
3. $D + D \longrightarrow {}^{3}_{2}\mathrm{He} + n + 3.27\ MeV$
4. $D + {}^{3}_{2}\mathrm{He} \longrightarrow {}^{4}_{2}\mathrm{He} + H + 18.3\ MeV$

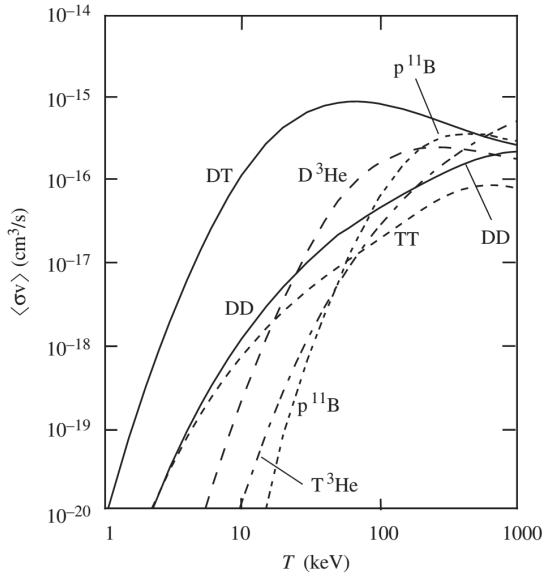

Figure 1.5: Reactivity of fusion reactions, plotted as a function of temperature [3].

The reaction with the highest cross section is the D-T reaction. For this reason, this is the reaction most suited to be exploited in a fusion reactor. Focusing on the D-T reaction, we observe that it consists in the fusion of a nucleus of deuterium and one of tritium, with the production of an α particle (He nucleus), a neutron and 17.6 MeV of energy. More precisely, this energy is divided as follows: the α particle has an energy of 3.5 MeV, and the neutron an energy of 14.1 MeV. For comparison, the fission of a uranium-235 nucleus yields around 200 MeV of energy, while the oxidation (combustion) of a methane molecule releases only 9.2 eV of thermal energy.

The simplest strategy to initiate fusion reactions involves accelerating a stream of ions of a particular kind to the required energy level and directing it toward a target composed of atoms of another type. Alternatively, two beams containing distinct ion types could collide head-on. Unfortunately, this approach is confronted with a significant challenge: the elastic collision cross section is at least two orders of magnitude greater than that for the D-T fusion reactions. Ions undergoing elastic collisions are lost from the beam, along with the energy expended to accelerate them. This barrier renders the achievement of a positive energy balance unattainable, where the energy generated exceeds the energy invested in ion acceleration. Therefore, the resolution lies in creating a plasma that encompasses both types of ions and effectively constraining it within a defined spatial domain for a significantly extended period, surpassing the duration of collisions. Through this approach, ions are granted ample time to engage in fusion reactions, devoid of being lost due to elastic collisions.

Focusing again on D-T reactions, D is a stable isotope of hydrogen, we can find it present in water in a proportion of 1 part over 6700 of H, therefore it can be considered as a virtually inexhaustible fuel. On the other hand, T is a radioactive[3] element with a half-life ($t_{1/2}$) of 12.3 years. This means, it is extremely rare to find tritium in nature and require a method to produce it. The presently foreseen method consists of exploiting the neutrons produced by the fusion reactions to *fertilise* lithium, according to the reactions:

1. $^{6}\mathrm{Li} + n \longrightarrow T + {}^{4}_{2}\mathrm{He} + 4.8\ MeV$
2. $^{7}\mathrm{Li} + n \longrightarrow T + {}^{4}_{2}\mathrm{He} + n - 2.5\ MeV$

Due to the cross sections, fast neutrons with energy larger than 3 MeV interact mainly with ^{7}Li (main isotope, abundance of 92.6%), while slower neutrons interact with ^{6}Li (abundance of 7.4%). The reactor will thus use as primary fuel deuterium and lithium. The practical realization of lithium transmutation into T requires the positioning around the plasma of a blanket containing lithium. This is the working principle of the so-called *breeding blanket*. The Blanket is traversed by pipes where a cooling fluid will circulate, extracting the heat released by the neutron flux and bringing it to a heat exchanger, where it will be used to produce steam. The steam, through another circuit, drives a turbine connected to a generator in order produce electricity (figure 1.6).

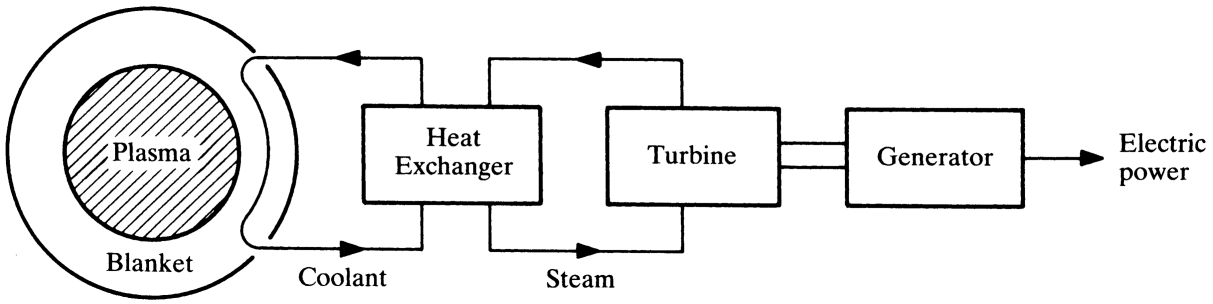

Figure 1.6: Scheme of the fusion reactor parts devoted to electricity production [3].

[3]A radioactive decay is the process by which an unstable atomic nucleus loses energy by radiation. A material containing unstable nuclei is considered radioactive.

1.1.3 Magnetic Confinement Fusion: an approach to generate fusion power

The basic principle of a fusion reactor is to be able to confine ions for a sufficiently long time and at sufficiently high density. Furthermore, it must be able to heat the reagents to temperatures[4] of the order of 10 keV (100 million degrees) to trigger the reactions: depending on the conditions reached, the heating can be subsequently switched off, if ignition is reached, or must be kept on during the reactor operation.

One of the most crucial issue consists in the plasma confinement. Apart from the gravitational confinement, method used in the reactors built by nature, such as our Sun and other stars, there are 2 conceptual research lines on Earth: magnetic confinement and inertial confinement.

- In the 1940s, an innovative type of approach, the magnetic confinement approach started to become important in order to research nuclear fusion power. *Magnetic confinement fusion* is an approach to generate thermonuclear fusion power that uses strong magnetic fields to confine fuel in the form of a ionized plasma; the kinetic pressure of the plasma results balanced by the magnetic field, confining it to a fixed volume. This will be the method of consideration.
- A further approach consists in focussing very powerful lasers onto tiny spheres of solid D-T mixtures in order to reach fusion temperatures and densities. The external layers vaporise, compressing the internal parts and increasing the core density and temperature to fusion levels. Fusion reactions are then confined by the laser-induced shock waves coming from the external layers. Considering a spherical target of radius R with mass density ρ and temperatures of few tens keV, the condition required is:

$$\rho R > 3 \ g/cm^2 \tag{1.3}$$

  confirming the necessity of achieving high fuel compressions. A target radius of 15 cm would be required when using solid deuterium whose density is of 0.2 g/cm^2. This method is called *inertial fusion*.

In order to produce electricity, both for magnetic confinement and inertial fusion, the energy balance of a reactor has to be positive, the energy produced by fusion reactions has to exceed that required to create and sustain the plasma itself. The power balance equation is composed of different contributions:

$$\frac{dw}{dt} = p_H + p_\alpha - p_L - p_R \tag{1.4}$$

The quantity $w = 3nT$ corresponds to the plasma thermal energy density (in plasma physics k_B is implicit inside T), p_H and p_α are the external heating power and the self-heating power from α particles respectively, while p_R and p_L represent the power losses from radiation (mainly from *Bremsstrahlung*[5]) and transport processes.

We can express the total power production from fusion reactions as:

$$p_f = \frac{1}{4} n^2 \langle \sigma v \rangle_T E_f \tag{1.5}$$

where $n = n_D = n_T$ is the D-T mixture density, which is considered to be the same both for deuterium and tritium; $E_f = 17.6$ MeV is the energy output from a single fusion reaction and the product $\langle \sigma \mathrm{v} \rangle_T$ is the Reactivity, as already introduced. This quantity is proportional to the number of reactions occurring per unit volume and time and is dependent on temperature.

[4]The temperature is usually expressed in electronvolts (eV), meaning by this k_BT with the temperature in Kelvin (K) and the Boltzmann constant ($k_B = 1.380649 \times 10^{-23}$ JK^{-1}): 1 $eV = 1.6022 \times 10^{-19}$ J, it corresponds to a temperature of about 11600 K.

[5]The *Bremsstrahlung* (from German *bremsen*: to brake and *Strahlung* : radiation) is an electromagnetic radiation produced by the deceleration of a charged particle when deflected by another charged particle; this could typically be an electron by an atomic nucleus. The radiation, such as photon, comes from the loss of kinetic energy of the moving particle, the whole process satisfies the law of conservation of energy.

A typical value for this last quantity is $\langle \sigma \mathrm{v} \rangle_T = 1.1 \times 10^{-24}\ T^2 m^3 s^{-1}$ when considering temperatures of around 10-20 keV for our mixture.
In magnetic confinement reactors around 4/5 of the output power escapes the confined plasma, used for the Blanket and heat production, as it is carried by neutrons, which do not interact with the magnetic fields, while the remaining 1/5 goes to α-particle heating.

Examining now the single contributions of the power balance equation, two negative terms stand out from it: radiation losses and transport losses. If we consider radiation losses, this is mainly composed of two cotributions: Bremsstrahlung and line radiation losses. As explained, the Bremsstrahlung in a plasma is due to numerous collisions between charged particles, making them decelerate and accelerate therefore emitting light. On the other hand, line radiation comes from impurities present in the plasma being excited and subsequently relaxing to a lower energy state.
Analysing transport losses, an empirical quantity, called *energy confinement time* τ_E, is introduced. If, ideally, one could switch off all the heating sources and radiation losses, the energy content would decay exponentially with a time constant equal to τ_E . An abundance of experimental evidence in various confinement modes shows that the energy confinement usually increases as one moves from hydrogen to deuterium or deuterium-tritium plasmas.
We define it as: $P_L = \frac{W}{\tau_E}$. where P_L and W are the power losses and the internal thermal energy, respectively.

Another crucial quantity worth mentioning in energy balancing equations, is the so-called Q-Gain value: $Q = \frac{P_f}{P_H}$. It basically describes the fusion energy output normalised to the heating energy input in the reactor. An important value is Q = 1, called *break-even*, in which fusion reactions produce a quantity of energy equal to that used to heat the plasma. It is easy to understand that when Q = 5, the α-particle energy is equal to the heating power, so that only half of the power losses needs to be compensated with external heating while the neutrons carry out of the plasma a power equal to $4p_H$. The ideal condition of $\mathrm{Q} = \infty$ corresponds to *Ignition*, in which $p_H = 0$, the plasma is fully self-heated by α particles .

Lastly, we deal with the *triple Product*, essential parameter leading to confinement. It is the product between plasma temperature, density and energy confinement time and embodies the performances of the particular experiment or reactor based on the process. Simplifying, for the 10-20 keV range and assuming flat temperature and density profiles:

$$nT\tau_E \geq 3 \times 10^{21}\ m^{-3} keV s \tag{1.6}$$

1.1.4 An experimental machine to harness fusion: the tokamak

The aim of fusion research is to seek the best conditions for plasma confinement. Several magnetic field geometries have been investigated, such as magnetic mirrors, linear and toroidal configurations. Among them, the toroidal geometry devices, the so-called tokamaks and stellarators, have given the best confinement performances.

When charged particles flow in the magnetic chamber, they are not allowed to explore the whole space freely, indeed the magnetic field affects the orthogonal velocity component constraining the particles to move in their Larmor orbits, around the so-called guiding centre, while the parallel component is not affected. A Larmor orbit is the motion of a charged particle in a uniform magnetic field, which is a superposition of uniform circular motion in a plane perpendicular to the field and uniform motion parallel to the field. Its radius is:

$$\rho_L = \frac{m v_\perp}{qB} \tag{1.7}$$

where q is the particle charge and $\mathrm{v}_\perp$ is the velocity component perpendicular to the magnetic field. The particle results confined in the two directions perpendicular to the sufficiently large field, since the Larmor radius must be substantially smaller than the size of the chamber. As the temperature increases also the required magnetic field will increase.

The most effective approach to avoid longitudinal losses, as with the magnetic mirror effect, is to close the magnetic field lines on themselves, forming a doughnut-shaped configuration, geometrically called a torus. The simplest way to achieve such a magnetic field is to use coils placed so as to form a toroidal solenoid. However, such a configuration still displays modest confinement properties, due to the fact that the field generated by the toroidal solenoid is not uniform, but decays with the distance R from the torus major axis as 1/R, as can be easily shown applying the integral form of Ampère's law to a circular path inside the torus itself.

A single particle's motion in a magnetic field with spatial variations in magnitude and direction can be studied, the results reveal that slow drift motions are superposed to the fast spiral motion. It is possible to demonstrate that the centre of the circular orbits travels not only in the direction parallel to B, as in the uniform case, but also in the perpendicular one, with certain drift velocity (vector quantities are indicated in bold):

$$\mathbf{v_D} = \frac{mv_\perp^2}{2qB}\frac{\mathbf{B}\times\nabla B}{B^2} + \frac{mv_\parallel^2}{qB}\frac{\mathbf{R_C}\times\mathbf{B}}{R_C^2 B} \tag{1.8}$$

where m and q are the mass and charge of the particle, $v_\perp$ e $v_\parallel$ are its velocity component perpendicular and parallel to the magnetic field and R_C is the field curvature radius. In the case of the toroidal solenoid, a vertical drift motion in the z-direction takes place, with opposite directions for ions and electrons, with subsequent charge separation. This leads to the formation of a vertical electric field. The combination of the two fields produces a further drift motion directed towards the outer part of the plasma torus:

$$\mathbf{v_D} = \frac{\mathbf{E}\times\mathbf{B}}{B^2} \tag{1.9}$$

The cause of the poor confinement is the drift motion, equal for both species.

This issue can be resolved by superposing a poloidal magnetic field component $\mathbf{B}_P$, which can be produced by a current $\mathbf{I}_P$ running within the plasma itself or by additional external coils, to the toroidal magnetic field component $\mathbf{B}_\phi$, generated by the coils. Field lines encircle the torus helically as a result of the superposition of the two components. Particles will alternately be found in the top portion of the torus, where the vertical drift will drive them away from the equatorial plane and in the lower part, where the drift will move them towards the equatorial plane. This motion of the particle orbit centres will also be helical. In the end, because of these opposing contributions, the effects of the drift motion will cancel out when the particle does a full poloidal rotation.

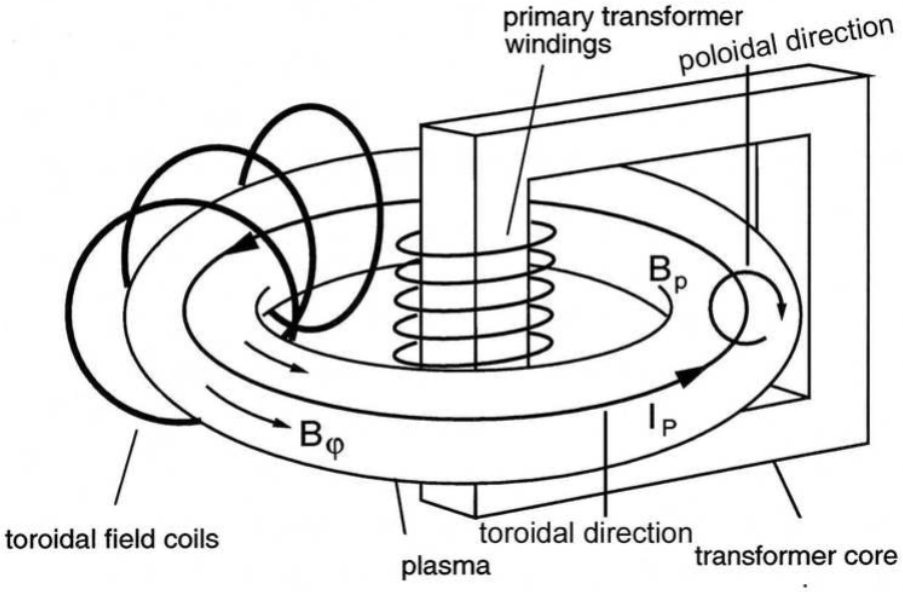

Figure 1.7: Representation of principal components of a tokamak [13].

First developed by Soviet research in the late 1960s, the tokamak has been adopted around the world as the most promising configuration of magnetic fusion device.
The name tokamak is a Russian acronym which stands for *Toidalnaya Kamera* and *Magnitnaya Katushka* (toroidal chamber and magnetic coil). The heart of a tokamak is its doughnut-shaped vacuum chamber. Inside, under the influence of extreme heat and pressure, gaseous fuel becomes plasma, which is a hot, electrically charged gas. Figure 1.7 represents the structure of a tokamak with its main components.

On the other hand, the magnetic cage of a stellarator is produced with a single coil system, without a longitudinal net-current in the plasma and therefore without a transformer. This makes stellarators suitable for continuous operation, whereas tokamaks without auxiliary facilities operate in pulsed mode.

To start the process, air and impurities are first evacuated from the vacuum chamber and the magnet systems that will help to confine and control the plasma are charged up and the gaseous fuel is introduced. As a powerful electrical current is run through the vessel, the gas breaks down electrically, becomes ionized (electrons are stripped from the nuclei) and forms a plasma. As the plasma particles become energized and collide they also begin to heat up.

The charged particles of the plasma can be shaped and controlled by magnetic coils placed around the vessel; physicists use this important property to confine the hot plasma away from the vessel walls. Auxiliary heating methods help to bring the plasma to fusion temperatures (between 150 and 300 million °C). Particles "energized" to such a degree can overcome their natural electromagnetic repulsion on collision to fuse, releasing huge amounts of energy.

Toroidal current by itself can be driven in many ways, but the main mechanism relies on current induction as in a transformer. For instance every tokamak behaves as a giant transformer, as showed in the picture, where coupling takes place between the central solenoid, acting as the primary circuit, and the toroidal plasma current, acting as the single secondary current circuit.

We introduce a fundamental parameter:

$$\beta = \frac{p}{p_{mag}} \tag{1.10}$$

ratio between $\mathrm{p} = \mathrm{n}k_B\mathrm{T}$, the plasma pressure and $\mathrm{p}_{mag} = \mathrm{B}^2/2\mu_0$, the magnetic pressure. The parameter can be considered as an indicator of the reactor efficiency, to take into account when considering fusion plasmas confined by strong magnets.
The magnetic field that appears in the formula is normally the total field. In tokamaks, where the magnetic field is the sum of two components, one toroidal and one poloidal created by the plasma current, "poloidal beta" is often used to characterise the MHD stability of the system and the toroidal one to characterise the confinement properties. In tokamaks, the beta value in the vast majority of cases does not exceed 6%, which is a relatively low value. This means that only 6% of the pressure due to the magnetic field is converted into plasma pressure, i.e. confinement.

Having two components, magnetic field lines are thus helixes which wind around the torus, see figure 1.8 . These lines close on themselves and a set of them defines a so-called magnetic flux surface, nested one into another. Helical magnetic field lines are described by the *Safety Factor, q*, which is defined as the ratio between the angular distance a field line has to toroidally travel before reconnecting, hence completing a full poloidal turn. The name safety factor comes from the fact that this quantity is crucial to determine several features of the plasma instabilities. It can be linked the torus radii and the magnetic profiles as:

$$q(r) \approx \frac{rB_\phi(r)}{R_0 B_P(r)} \tag{1.11}$$

where r is the minor radius of the flux surface and R_0 is the torus major radius. An important parameter for the stability of the plasma is the safety factor at 95% of the magnetic flux q_{95}, usually it denotes an unstable plasma for values less or equal than 2.

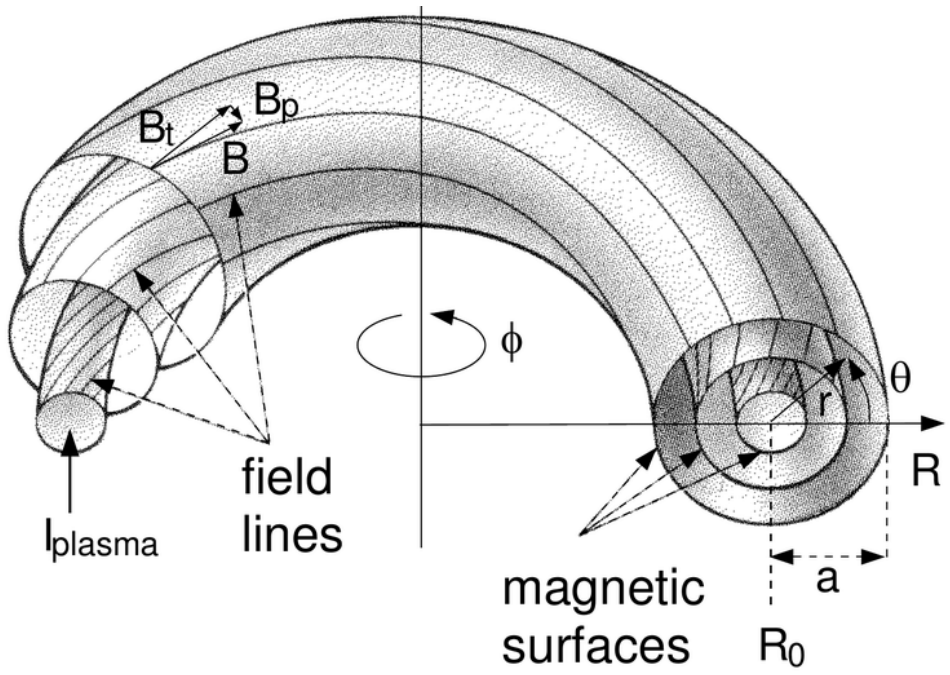

Figure 1.8: Geometry of the magnetic field lines and nested magnetic flux surfaces in a toroidally symmetric tokamak plasma [12].

In order to handle the plasma-wall interaction and the recycling, appropriate objects are used as preferential interaction regions. According to their characteristics, the two possible configurations (see figure 1.9) in which the plasma comes into contact with the vessel wall, depending on the shape of the magnetic flux surfaces are:

- the *limiter*, a solid object protruding from the inner surface of the vacuum chamber, which modifies the plasma-wall interaction, confining it to a narrow area while also protecting the vessel. The plasma erodes the limiter material because to its high temperatures, increasing the number of impurities diffusing into the plasma. These contaminants can radiate a significant portion of the plasma energy, causing the plasma to cool and in the worst-case scenario, disrupting the plasma current. This configuration has become less important because the divertor configuration has proved to be more favourable for good plasma confinement;

- the *divertor*, situated at the bottom of the vacuum vessel, consists in extra magnetic coils that create a null point, called X-point, in the poloidal magnetic field near the edge of the plasma. The plasma diffuses from the confined region over the separatrix, which defines the last closed flux surface (LCFS), to the region of open field lines. Both particles and energy are rapidly lost down the field lines and can reach the divertor targets. Because of the high parallel to perpendicular transport ratio, just a tiny layer of plasma with radial extension of ≈ 1 cm, known as the *scrape off layer* (SOL) connects the separatrix to the divertor targets.
  The advantage is that this configuration provides superior impurity isolation due to the distance between the divertor and the confined plasma. The structure can be adjusted to create a high neutral pressure, allowing for more efficient particle pumping near the divertor plates than in a limiter situation. Furthermore, the divertor helps in lowering the power loads by radiation, lowering the temperature of the plasma. When the temperature falls below around 5 eV, the divertor enters a state known as detachment. Atomic processes diminish particle flux to divertor targets at these conditions. When compared to the attached regime, the detachment is a more advantageous regime because the reduced power and particle loads can lengthen the life of the divertor's materials. Finally, the divertor facilitates plasma entry to the H-mode regime, as we will see. Its disadvantage is of requiring a larger volume of the vacuum chamber and focusing the heat load on a restricted portion of the divertor target.

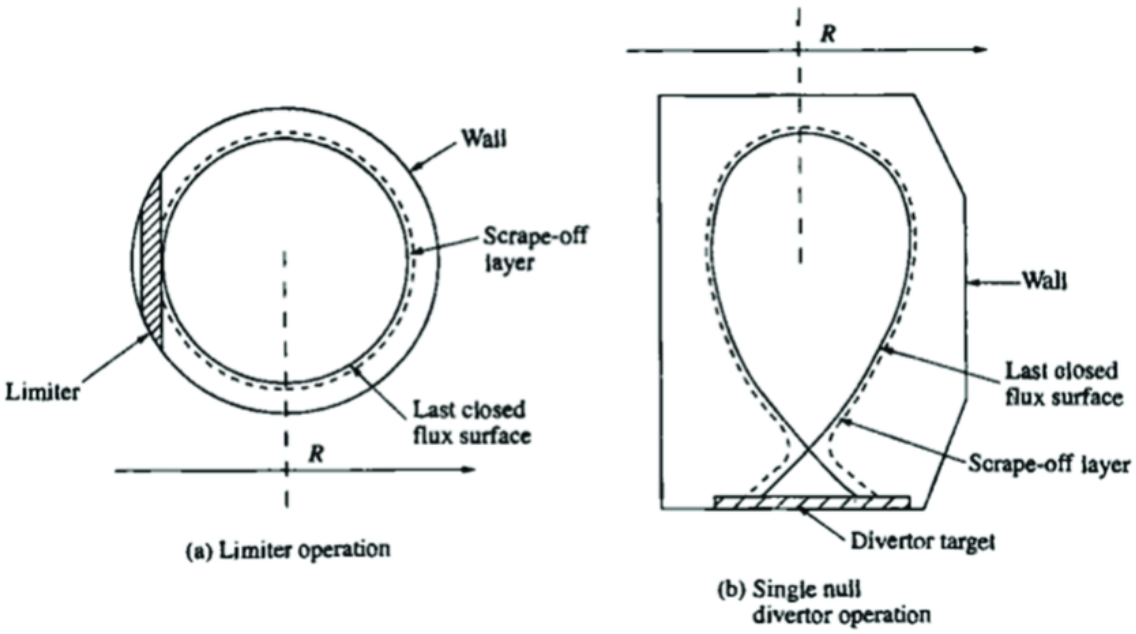

Figure 1.9: Poloidal cross-sections of a tokamak in the Limiter (a) and in the divertor (b) configurations [3].

One of the most ambitious energy projects in the world today is ITER (International Thermonuclear Experimental Reactor or "The Way" in Latin). ITER will be the world's largest tokamak, it will be, in linear dimensions, twice the size of the largest machine currently in operation, with ten times the plasma chamber volume. The construction is situated in southern France, where 35 nations are collaborating.

1.1.5 ASDEX Upgrade: a divertor tokamak

ASDEX Upgrade (AUG) (*Axially Symmetric Divertor Experiment*) is a divertor tokamak at the Max-Planck-Institut für Plasmaphysik (IPP), Garching (Germany). It is, compared to other international tokamaks, a midsize tokamak experiment. A sketch of its structure is shown in figure 1.10. It began operation in 1991 and it succeeded the ASDEX experiment, which was in operation from 1980 until 1990. At present, it is Germany's second largest fusion experiment after the stellarator Wendelstein 7-X at Max-Planck-Institut für Plasmaphysik in Greifswald, Germany.

ASDEX Upgrade's overall goal is to establish the scientific basis for the optimisation of the tokamak approach to fusion energy and especially to prepare the next steps: ITER and DEMO[6]. For this purpose essential plasma properties, primarily normalised plasma density, plasma pressure and the wall load, are matched to the conditions in a future fusion power plant.

Innovative is its all tungsten (high Z[7] material) first wall. tungsten proves to be an optimal selection for the initial wall of a tokamak due to its elevated melting point, surpassing 3000 °C. This attribute empowers it to endure the intense heat fluxes emanating from the hot plasma located at the core of the tokamak. However tungsten has the tendency to ionise at high temperatures, "polluting" the plasma and diluting the deuterium-tritium fuel mix. Furthermore, radiation from fully ionized tungsten, is several orders of magnitude higher than that of other proposed first wall components such as Carbon fibre composites or beryllium. This result, allows for far less Tungsten to "contaminate" a proposed break-even plasma.

A list of the technical specifications follows in 1.1 [41].

[6]DEMO refers to a proposed class of nuclear fusion experimental reactors that are intended to demonstrate the net production of electric power from nuclear fusion.

[7]The atomic number or nuclear charge number (Z) of a chemical element, is the charge number of an atomic nucleus. This is equal to the proton number or the number of protons found in the nucleus of every atom of that element.

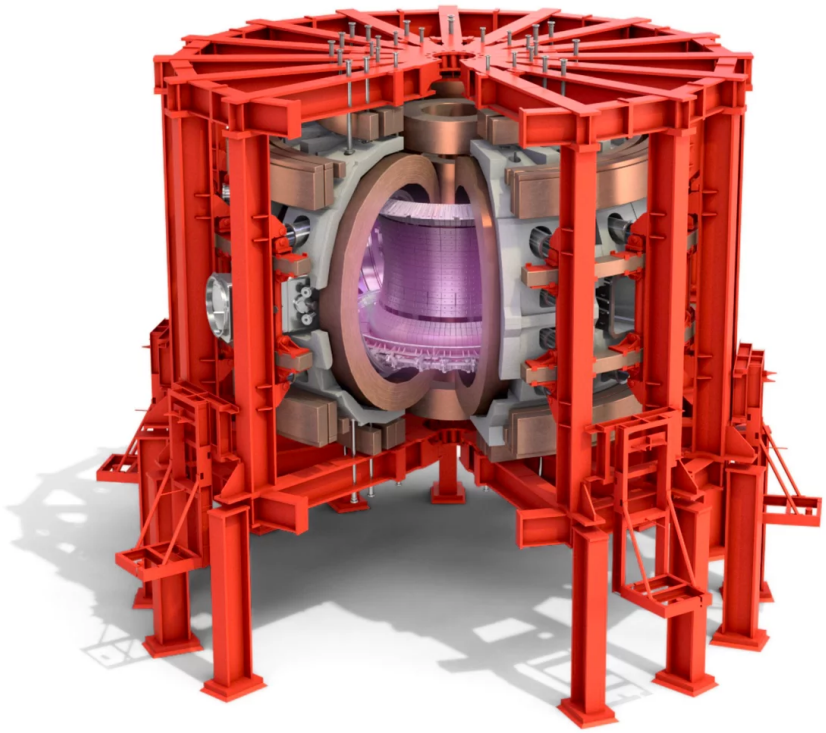

Figure 1.10: Sketch of the ASDEX Upgrade fusion device in Garching, Germany. From the interior to the exterior: plasma, plasma vessel, main field coils, poloidal field coils and support structure [41].

TECHNICAL SPECIFICATIONS	**VALUES**
Total height of the device	9 m
Major plasma radius	1.6 m
Minor plasma radius	0.5 - 0.8 m
Magnetic field	3.2 T
Plasma current	1.4 MA
Pulse length	10 s
Plasma heating	27 MW
Plasma volume	13 m^3
Plasma quantity	3 mg
Plasma mixture	H, D, He
Plasma temperature	10^8 °C
Plasma density	2×10^{20} particles per m^3

Table 1.1: Technical specifications of ASDEX Upgrade.

Plasma heating and current drive in AUG are derived from several sources. The toroidal magnetic field is generated by 16 large copper magnet coils wrapped around the ring-shaped plasma vessel. Also, auxiliary coils, for the divertor, the plasma current, the shaping and positioning of the plasma, are present. The experiment weighs 800 tons. A wide variety of plasma properties are recorded, with 40 diagnostics. Up to 4 gigabytes of raw data is stored per discharge. The measurements results are available in real time for feedback control of the plasma. The electrical energy for supplying the magnetic field coils and the plasma heating systems are provided by large flywheel generators.

ASDEX Upgrade avoids the utilization of radioactive T as fusion fuel. Fusion reactions are induced within the model plasma utilizing H, D and He, even if rare. To safeguard against the fusion neutrons generated in this process, the facility was constructed within a hall furnished with concrete walls measuring 2 m in thickness and a roof measuring 1.80 m in thickness. This design effectively captures the annual production of up to a maximum of 10^{19} neutrons. The device's activation remains minimal and undergoes rapid decay, permitting access to the experiment during non-operation periods.

Since the end of July 2022, the counter in the ASDEX Upgrade control room has read 41570 plasma discharges and it won't change for another two years. ASDEX Upgrade is currently getting ready for its upcoming mission, which involves testing a new divertor design in which the magnetic flux tubes are flared close to the power-receiving wall sections or near the divertor. Cryopumps, a new upper divertor to replace the previous upper divertor and two concentric in-vessel coils must all be fitted for this purpose.
If all goes as planned, AUG will restart its trial operations in July 2024 [47].

The closest to a burning plasma has been achieved by the European Community's JET device, in Oxfordshire, UK, which has been, up to now, the largest fusion experiment in the world.
In figure 1.11, different fusion experiments are compared, considering the triple product (10^{17} particles per $cm^3 \times s \times °C$) in function of their temperatures.

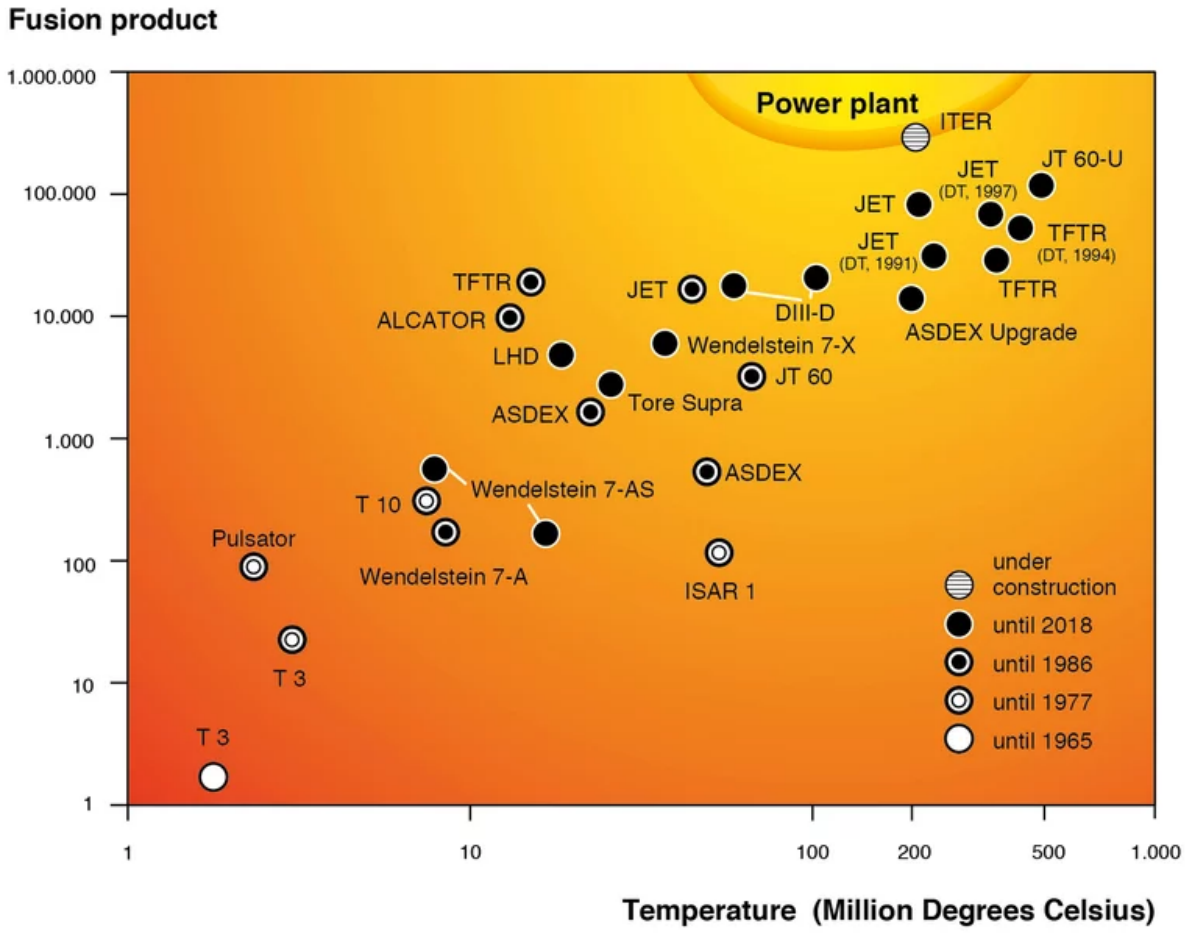

Figure 1.11: Ignition diagram showing the progress of fusion research [41].

Chapter 2

Theoretical overview

The second chapter deals with a theoretical overview of the structure of the pedestal, a zone of steep temperature and density gradients, which is limited by edge localized modes (ELMs). The linear stability of these modes is well described by the theory of ideal magnetohydrodynamics (MHD) [7], [8].

2.1 Pedestal: H-mode effect

The usual operating regimes for magnetic confinement fusion devices are the low confinement mode (L-mode) and the high confinement mode (H-mode). Friedrich Wagner and his colleagues found the H-mode in 1982 while applying neutral-beam heating to the plasma at ASDEX. The H-mode was named after the improved confinement regime, whereas the L-mode was named after the preceding state of lower confinement. H-mode enables improvement of confinement times by a factor of nearly 2 in comparison with L mode. It has since been replicated in all major toroidal confinement devices and it is still today the reference scenario for the next step machine ITER.

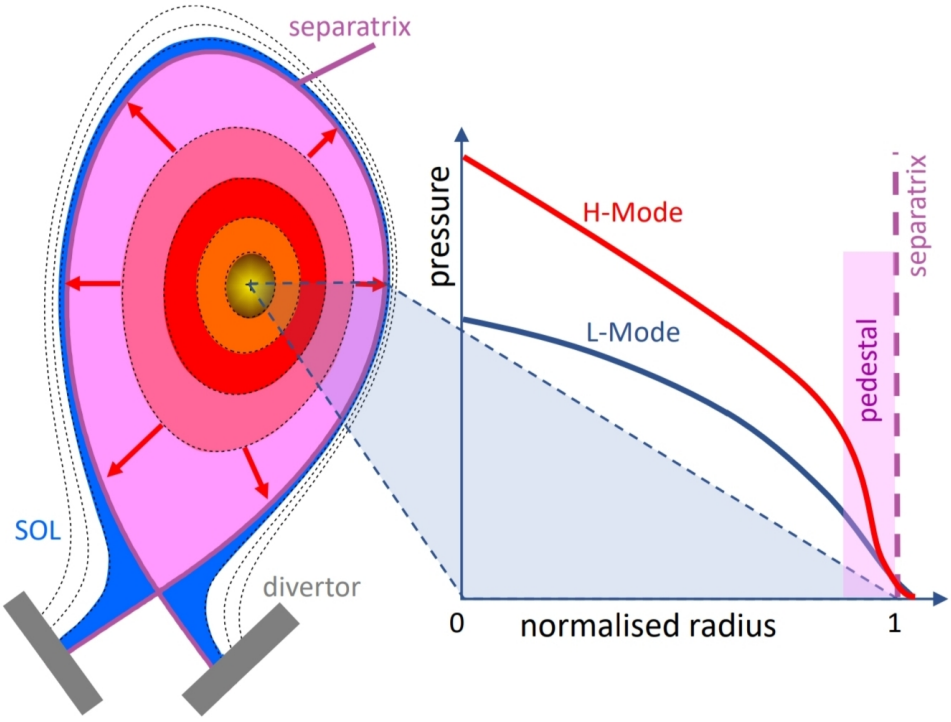

Figure 2.1: Poloidal cross section of the nested flux surfaces of a divertor plasma with a comparison of radial L and H-mode pressure profiles and an emphasis on the scrape-off layer (SOL), separatrix, divertor and pedestal [19].

When the provided heating power exceeds a specific threshold, the plasma spontaneously transitions into a higher-confinement state in which the energy confinement time roughly doubles, yet continues with an inverse relationship on heating power. In the proximity of the separatrix, the increased confinement stems from the edge of the confined plasma. A layer of plasma with excellent thermal insulation properties of a few centimetres thick, displays considerably reduced perpendicular transport due to an *edge transport barrier* (ETB), resulting in the formation of steep temperature and density gradients. The steep gradient zone is known as a *pedestal* since it resembles a structure elevating the core profiles. During this transition, the temperature core gradient length $|\nabla T|/T$ is normally constant, known as profile stiffness.

Figure 2.1 shows on the left a poloidal cross section with relative nested flux surface of a divertor plasma and on the right the pressure in function of normalised radius graph displaying a comparison between H-mode an L-mode. The pedestal area with its steep gradient zone and delimited by the separatrix is clearly visible.

Scaling laws, empirical laws deduced from experimental data linking the energy confinement time to the plasma parameters, have been formulated for L-mode and H-mode plasmas, showing a decrease of the energy confinement time with heating power.
A useful parameter to quantify the goodness of an H-mode is the H factor, which is defined as the ratio of the achieved experimental energy confinement time with that predicted for the same conditions by the scaling laws:

$$H = \frac{\tau_{E,exp}}{\tau_{E,scaling}} \tag{2.1}$$

It is also possible to see that the consequence of the pedestal is that the central density, and the average density, are increased; the same thing holds for the temperature.

The processes underlying the formation of the ETB are still unknown and are the subject of a number of both theoretical and experimental studies. Even if H-mode was discovered by chance, we now know that turbulence stabilisation, which is the cause of confinement deterioration, is achieved through a differential in the poloidal rotation velocity of the different magnetic surfaces (velocity shear). The magnetic surfaces are indeed rotating as a consequence of the plasma electric fields. A change in these electric fields creates a velocity shear, which prevents turbulence from forming. At the plasma edge, a transport barrier is formed, which keeps heat and particles in its core. The establishment of large gradients in the plasma edge is the most distinguishing feature of these situations, leading to the formation of a pressure pedestal in the plasma that is proportional to its density and temperature. The H-mode is steeper at the edge zone than the comparable L-mode curve.

2.1.1 Edge localized modes

During the H-mode, it is usual to see quasi-periodic explosive events at the plasma edge which expel particles and energy on millisecond time-scales, leading to a transient degradation, instabilities and expulsion of a burst of mass and energy from the plasma. This happens when plasma transition to high confinement state. These events are known as *edge localized modes* (ELMs) and are intensively studied since they must be kept at a relatively low magnitude in a reactor to avoid damaging the plasma-facing components. They are to be considered as responsible for limiting the pedestal height.

Regularly, the plasma pressure profile relaxes towards less steep slopes. The barrier then re-emerges and the profile steepens again before collapsing at the next ELM. As a result, at each ELM, large particles and heat blasts escape from the plasma, limiting the vacuum chamber components.

ELMs are categorised in different types depending on their frequency and associated energy loss.

We mainly consider three different types.

- Type I ELMs emerge at high edge temperatures and can occur over a large range of the tokamak operational space. They degrade the transport barrier leading to energy and particle loads on the vessel material. This could result in severe damage. The theory of ideal magnetohydrodynamics (MHD) describes well the onset conditions for type I ELMs. This is consistent with the observation that the type I ELM frequency increases with crossing the separatrix heating power, since the build up of the edge gradients toward the critical value is accelerated;
- type II ELMs are observed in highly shaped plasmas with high separatrix density. They are more frequent and less severe compared to the previous ELM type;
- type III ELMs usually occur close to the L–H threshold power and are possibly described by resistive MHD instability. As the edge temperature rises and resistive effects are suppressed, the type III ELM frequency decreases until this ELM type completely vanishes and the plasma transitions to a type I ELM regime.

2.1.2 Ideal magnetohydrodynamics

Solving equations of motion which describe the state of a plasma is referred to as plasma modelling. Plasma models can be classified as single particle, kinetic, fluid, hybrid kinetic/fluid, gyrokinetic or as a system of many particles, among other categories.

A magnetised plasma is considered as a many-body system, which means that a set of around 10^{20} individual motion equations, all coupled through the electromagnetic interaction, would have to be solved. Some kind of mean field theory is necessary in order to get reasonable conclusions without computational inaccessibility.

In the following, we deal with the theory of magnetohydrodynamics (MHD), which describes the plasma, through macroscopic quantities, as a combination of charged fluids. MHD combines electromagnetic and hydrodynamic description of the plasma in order to obtain a comprehensive picture of both static states and dynamic processes.
If the mean free path length [8] and the Larmor radius are much smaller than the size of the system, then, as in fluid theory, the assumption is that there are sufficiently many particles in each fluid cell, all in equilibrium. We take into account that MHD is only a consistent description for dynamics perpendicular to the magnetic field, due to the fact that the previous assumptions aren't valid for the parallel to magnetic fields, where the mean free path usually exceeds the system size. If the timescale of interest is shorter than the current redistribution time in the plasma, then the plasma can be considered to be a perfect electrical conductor, simplifying Ohm's law; this results in ideal MHD.

For the typical case of a two-component plasma, one ion species plus the electrons, the system of two-fluid equations can be combined to give a set of one-fluid equations. The two species have large mass difference, meaning that the mass and momentum are mainly contained in the ions; electrons, which guarantee quasi neutrality, lead to an electrical current as their velocity differs from that of the ions. The final set of one-fluid ideal MHD equations is:

$$\partial_t \rho + \nabla \cdot (\rho \mathbf{v}) = 0 \tag{2.2}$$

$$\rho \left(\partial_t \mathbf{v} + (\mathbf{v} \cdot \nabla)\mathbf{v}\right) = -\nabla p + \mathbf{j} \times \mathbf{B} \tag{2.3}$$

$$\mathbf{E} + \mathbf{v} \times \mathbf{B} = 0 \tag{2.4}$$

[8] The mean free path is the average distance over which a moving particle travels before changing its direction or energy. This results typically from one or more successive collisions with other particles.

Equation 2.2 is the differential form of the *continuity equation*, depending on the mass density ρ, the centre of mass velocity $\mathbf{v}$ and the time t.
Equation 2.3 is the *force balance equation*, it contains the isotropic pressure p, the current density $\mathbf{j}$ and the magnetic field.
Equation 2.4 is the *ideal Ohm's law* which includes the electromagnetic properties; $\mathbf{E}$ is the electric field. We notice that the ideal MHD equations are obtained by assuming that the plasma has zero resistivity meaning that the right hand side of eq. 2.4 is simply equal to zero instead of $1/\sigma\ \mathbf{j}$ with σ as electrical conductivity. An important consequence of the ideal Ohm's law is the fact that magnetic flux is conserved when moving with the plasma.

Another classification is the distinction between ideal modes, which are the instabilities described within the framework of ideal MHD, that is a version of MHD where the resistivity is neglected, and resistive modes, which depend on the finite plasma resistivity. In general, it is possible to say that if a plasma is ideally unstable, it will be unstable also if finite resistivity is taken into account. Indeed, ideal modes are the most violent instabilities which can take place in a magnetized plasma, have very fast growth rates, and lead almost invariably to premature discharge termination. On the contrary, an ideally stable plasma can be unstable with respect to some resistive modes. Resistive modes do not necessarily bring to discharge termination, but have negative effects on plasma confinement, since they can modify the magnetic surface topology. In some situations, resistive modes can destroy the magnetic surfaces, giving rise to field lines which fill ergodically a region of space: in this region the confinement will be poor.

These 3 equations need to be combined with the 3 *Maxwell's equations*, where eq. 2.5 is *Gauss' law of magnetism* (the divergence of the magnetic field is a boundary condition while the divergence of the electric field is to be seen as default in quasi-neutral plasma, eq. 2.6 is *Faraday's law of induction* and eq. 2.7 is *Ampère's law* and with the *adiabatic closure assumption* eq. 2.8:

$$\nabla \cdot \mathbf{B} = \nabla \cdot \mathbf{E} = 0 \tag{2.5}$$

$$\partial_t \mathbf{B} = -\nabla \times \mathbf{E} \tag{2.6}$$

$$\mu_0 \mathbf{j} = \nabla \times \mathbf{B} \tag{2.7}$$

with μ_0 being the magnetic permeability of free space.

Introducing the adiabatic constant γ:

$$\frac{d}{dt}\left(\frac{p}{p^\gamma}\right) = 0 \tag{2.8}$$

This relation is only valid for scalar pressure with the vector component of pressure excluded.

Solving all seven differential equations could be a challenging task. That is why many restricting assumptions were previously imposed.

2.1.3 Stationary ideal MHD equilibrium

The equilibrium between the pressure of the plasma, which tends to expand the plasma and the magnetic field, which confines it, is described by the Grad-Shafranov equation derived from the equilibrium equation in ideal MHD, as we are going to see. Zero net forces acting on the plasma are required for equilibrium. If we set that the derivative with respect to time t is zero in the motion eq. 2.3, we obtain the force-balance equation:

$$\mathbf{j} \times \mathbf{B} = \nabla p \tag{2.9}$$

where the plasma pressure p is acting outwards and the magnetic field inwards. We can deduce that there is no pressure differential along the magnetic field lines and no radial current.

The magnetic flux function satisfies the equation:

$$\mathbf{B} \cdot \psi = 0 \tag{2.10}$$

meaning that the magnetic field is perpendicular to the flux and the magnetic field lines lie in surfaces of constant flux. The magnetic field lines are embedded into concentric magnetic flux surfaces with constant pressure. The flux surfaces are nested around the centre which is called the magnetic axis. The last closed flux surface, as already mentioned, is the separatrix.

The normalised radius consists in a radial coordinate used for pedestal studies.
We define the two radial coordinates as follows:

$$\rho_{pol} = \left(\frac{\psi - \psi_{axis}}{\psi_{LCFS} - \psi_{axis}} \right)^{1/2} \tag{2.11}$$

$$\rho_{tor} = \left(\frac{\phi - \phi_{axis}}{\phi_{LCFS} - \phi_{axis}} \right)^{1/2} \tag{2.12}$$

ψ corresponds to the poloidal magnetic flux and ϕ to the toroidal magnetic flux. The coordinate is null at the magnetic axis (the innermost magnetic surface) and assumes the value of $\rho = 1$ at the LCFS. Overall, it is usually sufficient to consider only the poloidal cross-section of p, T and n because parallel transport is far greater than perpendicular transport, assuming that on a flux surface, not only the pressure, but also the temperature T and density n of the plasma are constant. In the axisymmetric tokamak geometry, the description of these parameters is then reduced to one dimension.

The equilibrium equation of a plasma which describes the balance of the pressure gradient, poloidal and toroidal currents and of the fields is the Grad-Shafranov (GS) equation:

$$F \cdot d_{\hat{\psi}} F + \mu_0 R^2 \cdot d_{\hat{\psi}} p = \mu_0 R j_{tor} = -\Delta^* \hat{\psi} \tag{2.13}$$

with $F(\hat{\psi}) = RB_{tor}$ and $\hat{\psi}(R,Z) = \int_0^R B_Z(R,Z)R \, dR - \int_0^{R_M} B_Z(R,Z_M)R \, dR$.

The poiladal flux, defined with respect to the magnetic axis, is expressed as $\psi = 2\pi\hat{\psi}$; B_{tor} and j_{tor} are respectively the toroidal magnetic field and current density; B_Z is the vertical component of the magnetic field; the magnetic axis is located in (R_M, Z_M).

We have also introduced the Stokes operator in cylindrical coordinates:

$$\Delta^* = R\partial_R(1/R \cdot \partial_R) + \partial_Z^2. \tag{2.14}$$

As we will see, there are different numerical codes solving the Grad-Shafranov equation for a given pressure, current density profile and plasma boundary, one of them is HELENA.

Assuming that the nested surfaces form circles around the centre R_0, the pressure is a function of ψ, therefore it is constant on the flux surfaces.

The inner surface of the tokamak however has a smaller area than the outer surface, which means that there is a force pushing the plasma outwards. The peak in the plasma current induces an additional force that expands the torus. These forces are opposed by a vertical magnetic field. The poloidal magnetic field, created by the plasma current is lower on the outside than it is on the inside of the torus, which causes the centres of the flux surfaces to be shifted outwards. This is called the Shafranov shift, well visible in sketch 2.2.

A great importance in the determination of the magnetic surfaces is played by the boundary conditions, determined by the currents flowing in the coils specifically used for equilibrium control, plasma position and shape. These currents allow, for example, to obtain D-shaped plasmas, the ones more commonly used in modern tokamaks since they allow to reach higher pressure values for a given toroidal magnetic field.

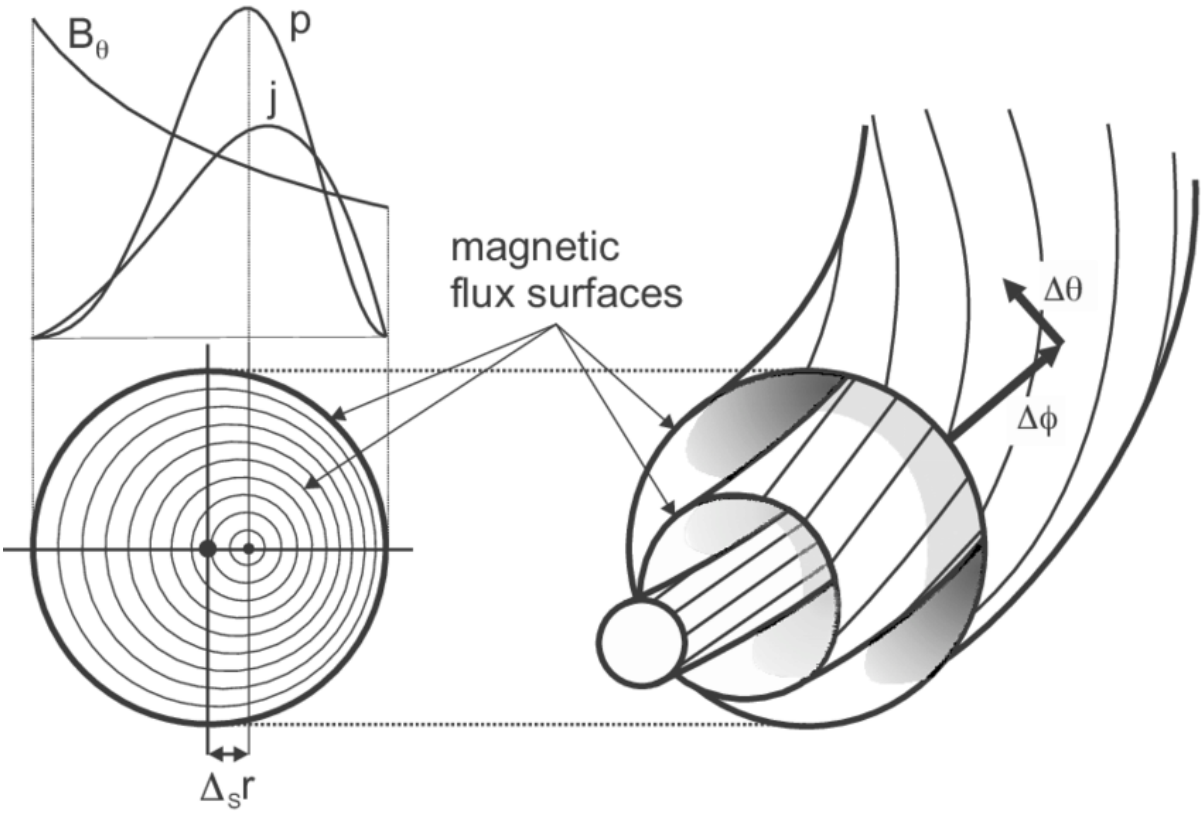

Figure 2.2: Nested flux surfaces in a toroidally and poloidally symmetric geometry for a limiter tokamak with the profiles of pressure, toroidal magnetic field, toroidal current density together with the Shafranov shift [20].

2.1.4 Linear MHD stability

The plasma is at equilibrium when the sum of all forces acting on it is equal to zero. Nonetheless, this does not imply that the plasma is to be considered as stable. Indeed, small perturbations could influence the equilibrium. The next approach consists in linearising the MHD equations around the equilibrium solution, obtaining, if $\mathbf{v_{eq}} = 0$:

$$\rho_0 \partial_t \mathbf{v}' = \frac{1}{\mu_0}((\nabla \times \mathbf{B_0}) \times \mathbf{B}' + (\nabla \times \mathbf{B}') \times \mathbf{B_0}) - \nabla p' \tag{2.15}$$

$$\partial_t \mathbf{B}' = \nabla \times (\mathbf{v}' \times \mathbf{B_0}) \tag{2.16}$$

$$\partial_t p' = -p_0 \gamma (\nabla \cdot \mathbf{v}' - (\mathbf{v}' \cdot \nabla) p_0. \tag{2.17}$$

Index 0 is for equilibrium quantities while ' is for small perturbations. Now, we introduce the perturbation ϵ where $\partial_t \epsilon = \mathbf{v}'$, the linearised flow-free MHD equations, eqs. 2.16 and 2.17, can be integrated and inserted into eq. 2.15.

The final result we get is:

$$\rho_0 \partial_t^2 \epsilon = \frac{1}{\mu_0}((\nabla \times \mathbf{B_0}) \times \mathbf{B}' + (\nabla \times \mathbf{B}') \times \mathbf{B_0}) + \nabla(p_0 \gamma \nabla \cdot \epsilon + \epsilon \cdot \nabla p_0) \tag{2.18}$$

with $\mathbf{B}' = \nabla \times (\epsilon \times \mathbf{B_0})$.

Integration bounds for t = 0 for $\mathbf{B}'$, ϵ', ρ' and p' are set equal to zero, while **v'** may be different from zero.

We can relate to a standard eigenvalue problem using an exponential Ansatz : $\epsilon(\mathbf{x}, t) = e^{-i\omega t}\epsilon_{spat}(\mathbf{x})$, depending on the spatial part of the perturbation. We also introduce the hermitian[9] MHD force operator $\mathcal{F}$:

$$-\omega^2 \rho_0 \epsilon = \mathcal{F}\epsilon, \quad \omega^2 \in \mathbb{R} \tag{2.19}$$

MISHKA is an example of numerical code which can solve this eigenvalue problem.

Moreover, the work done by the displacement δW$(\epsilon*, \epsilon)$ can be calculated, where $*$ denotes the complex conjugation. Also, the kinetic energy of the perturbation is introduced K$(\epsilon*, \epsilon)$:

$$\delta W(\epsilon*, \epsilon) = -\frac{1}{2}\int \epsilon* \cdot \mathcal{F}\epsilon dV = \frac{\omega^2}{2}\int \rho_0 |\epsilon|^2 dV = \omega^2 K(\epsilon*, \epsilon) \tag{2.20}$$

If K$(\epsilon*, \epsilon) \neq 0$:

$$\omega^2 = \frac{\delta W(\epsilon*, \epsilon)}{K(\epsilon*, \epsilon)}. \tag{2.21}$$

This last equation is valid even if ω is not an eigenvalue of eq. 2.19.

Using appropriate boundary conditions, an explicit form of the work functional may be derived for a magnetically confined fusion plasma in which the plasma volume is surrounded by a vacuum zone bounded by a perfectly conducting wall.

[9]The hermitian operator generalises the conjugate transpose of a square matrix to the infinite-dimensional case and the concept of the conjugate complex of a complex number.

We obtain that:

$$\delta W = \delta W_F + \delta W_S + \delta W_V \tag{2.22}$$

where the 3 terms are referred to fluid, surface and vacuum contributions.

If the current on the surface of the plasma is set to zero, which means that these contributions can be ignored in the context of minimisation, we can neglect the surface and vacuum term of the energy functional. Moreover, if we are only interested in modes that are localized inside the plasma edge, the ideal MHD energy functional is reduced to its fluid component:

$$\begin{aligned}\delta W_F = \int_{\text{Fluid}} \Bigg(\frac{|\mathbf{B}'_\perp|^2}{2\mu_0} + \left(\frac{|\mathbf{B_0}_{,\perp}|^2}{2\mu_0} |\nabla \cdot \epsilon_\perp + 2\epsilon_\perp \cdot \kappa|^2 \right) + \gamma p_0 |\nabla \cdot \epsilon|^2 - \\ - 2(\epsilon_\perp \cdot \nabla p_0)(\kappa \cdot \epsilon_\perp *) - \frac{j_{0,\parallel}}{|\mathbf{B_0}|} (\epsilon_\perp * \times \mathbf{B_0}) \cdot \mathbf{B}' \Bigg) dV\end{aligned} \tag{2.23}$$

with $\kappa = \mathbf{b} \cdot \nabla \mathbf{b}$ and $\mathbf{b} = \frac{\mathbf{B_0}}{|\mathbf{B_0}|}$ defining the curvature vector.

The first three terms of the fluid component can be associated respectively with energy of shear Alfvén waves[10], compressional Alfvén waves and sound waves, being always positive and thus stabilizing. The destabilizing parts of our fluid component are given by the fourth and fifth term, which represent the pressure-gradient driven and current-density driven instabilities. These last two terms can be negative.

More in detail, the pressure term is unstable if the pressure gradient and the curvature are parallel and stabilizing if they are anti parallel. The pressure gradient is perpendicular to the magnetic flux surfaces, pointing towards the centre of the plasma. The toroidal field curvature points towards the centre of the torus. The curvature of the magnetic field, often referred to as *good* or *bad* curvature, depending on the effect it has on the stability, results destabilizing at the outer half and stabilizing at the inner half of the torus. This kind of instability are called interchange instabilities due to the fact that the plasma tries to interchange position with the magnetic field.
This effect is particularly important on the outboard side; it causes the plasma to expand in this region, similarly to a balloon, that is why these type of instabilities are usually called *ballooning modes*.

Analysing now the current term, we see that it is proportional to the density of current parallel to the magnetic field. Magnetic surfaces kink as a consequence of current-driven instabilities. As a result, the kinked flux surfaces stretch the field lines, yet the kink can also locally lower the length, decreasing the plasma energy. The bootstrap current[11], rather than the ohmic current, is frequently the principal contributor to the current responsible for these instabilities in H-mode, because it is proportional to density and temperature gradients, which are typically substantial in the pedestal region. These instabilities are usually called *peeling modes* due to the fact that the plasma surface looks like *peeled off* by such kink.

The MHD stability of the pedestal can be described by the coupling of these two instabilities, hence the name peeling-ballooning modes (PBM). Linear ideal MHD codes scanning a range of possible finite mode numbers like MISHKA can then be used to calculate the PBM stability of a pedestal, taking as input the pressure, the current density, the magnetic flux profiles and the geometry of the LCFS.

[10] An Alfvén wave is a low-frequency, compared to the ion gyrofrequency, travelling oscillation of the ions and magnetic field in a plasma.

[11] The bootstrap current is a neoclassical toroidal current produced in the presence of a pressure gradient, associated with the existence of trapped (banana) particles in toroidal magnetic confinement systems. More details follow in the next chapter.

Chapter 3

Methods, tools and workflow

The third chapter presents the main plasma diagnostics at AUG and the profile fitting tools IDA (Integrated Data Analysis) and AUGPED employed for the automation of the workflow used to perform results for the MHD stability analysis of the pedestal for each discharge studied.

3.1 Diagnostics

In order to study the plasma behaviour and properties, a variety of methods, instruments and experimental techniques, called diagnostics, are necessary. These can monitor the plasma in ASDEX Upgrade (AUG). Precise evaluations of many plasma parameters, such as temperature and density, are enabled by their high time and spatial resolution. The experimental measurements of the diagnostics can be combined and processed in many ways in order to obtain radial profiles of the plasma quantities. The used technique depends on the kind of application. These are represented, as an example for AUG, in the sketch 3.1, for the discharge #33173 at time 3.7 s, in poloidal and toroidal cross sections.
A quick overview of the main diagnostics used to plot the profiles required for the analysis follows.

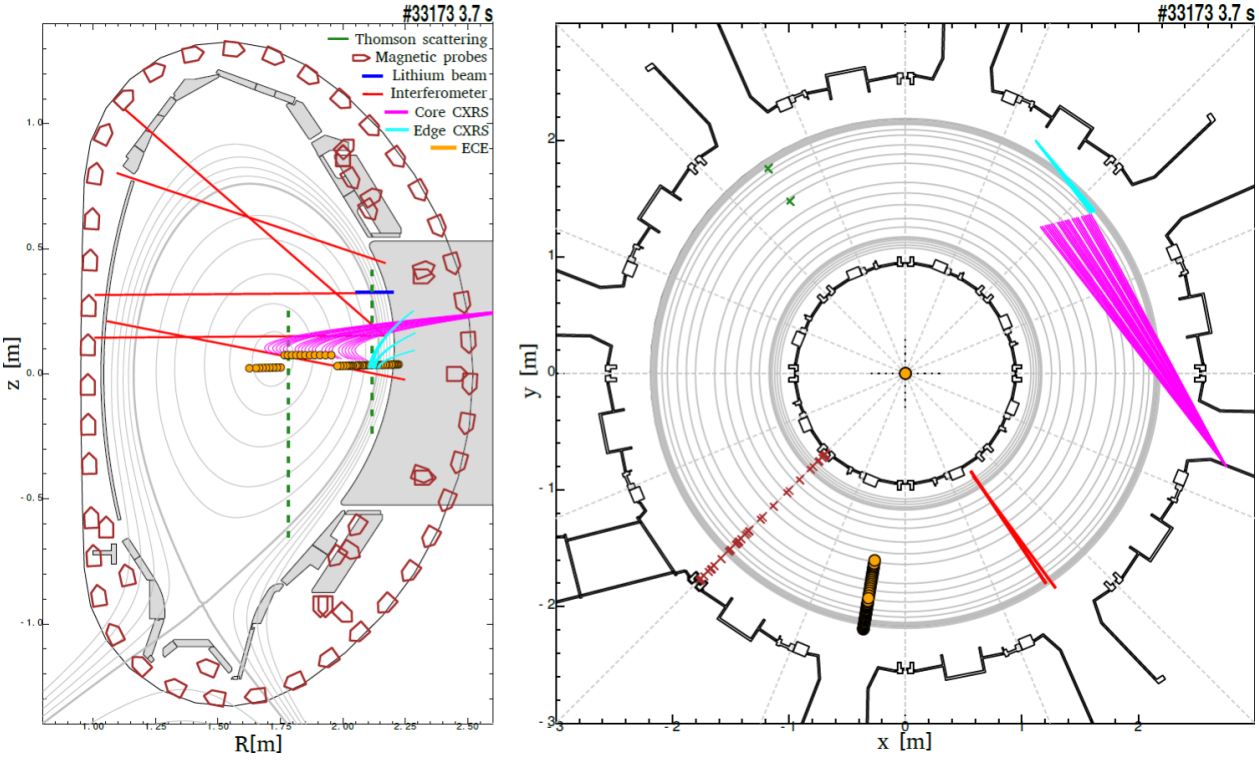

Figure 3.1: Main diagnostics considered both in poloidal (left) and toroidal (right) cross sections of AUG vessel. The locations and the lines of sight are well visible in different colours. [14].

3.1.1 Measurements of n_e and T_e

Thomson Scattering

The temperatures and densities of electrons in the plasma (n_e and T_e) can be measured at the same location with high accuracy by detecting the effect of Thomson scattering (TS) of a high-intensity laser beam. In any case, TS could be affected by the accuracy of its calibration. Given this characteristic of simultaneous measurements, TS can be used for the alignment of profiles relative to each other when combining the measurements from multiple diagnostics. TS is an active radiation measurement.

When a laser beam travels through the plasma, the electromagnetic field of the incoming light accelerates charged particles (in the specific case of plasma the electrons since $m_e \ll m_i$), causing them to generate electromagnetic waves of the same frequency but at a different angle. The thermal motion of electrons generates Doppler broadening of the spectra of emitted radiation, which can be used to determine T_e while the radiation intensity results proportional to n_e.

There are two vertical TS systems in AUG, one is for probing the core region and the other for the edge region of the plasma; furthermore a cluster of four, for the core, and six, for the edge, neodymium-doped yttrium aluminium garnet (Nd-YAG) lasers with wavelength 1064 nm, pulse energies of 1 J, pulse duration of 15 ns and repetition rate of 20 Hz is used. The scattered light is detected by 16 channels for the core and 10 channels for the edge (spatial resolution of 25 mm and 3 mm respectively). Also, TS has a high temporal resolution.

3.1.2 Measurements of n_e

Lithium Beam

Information on electron density n_e at the edge of the plasma can be obtained by measuring the interaction of injected neutral lithium (Li) atoms with the plasma [16]. As the Li beam injected into the plasma soon attenuates due to atomic processes, this approach can only measure near the plasma edge. Measurements are to consider no more reliable when we have higher densities, indeed, the beam penetrated into the plasma less in this situations because of the higher attenuation. At higher densities the beam penetration is even lower resulting in reliable measurements only at the very edge of the plasma.

High voltages are applied to extract lithium ions from a eucryptite emitter and accelerate them to energies ranging from 30 to 60 keV. After that, the ion beam is neutralized and introduced into the plasma. When neutral atoms come into contact with plasma, they become excited or ionised due to he collisions between the Li atoms, electrons and main ions. The most abundant excited state is Li(2p). This spontaneously decays in the Li(2s) state in 27 ns emitting a characteristic Li photon (wavelength of 670.8 nm). The Li transition's line radiation is filtered from the total radiation spectrum, then the signal is detected using photomultipliers. The measured light intensity is proportional to the electron density.

In AUG there are two optical systems (5 and 6 mm spatial resolution) to view the emission profile with a maximum time resolution of 200 kHz.

Interferometer

Interferometry is an active radiation measurement. The line integrated density along a line of sight can be determined by interferometry [17]. In AUG, a Mach-Zehnder interferometer is employed, which consists of a light beam in the far infrared (IR) range splitting into a reference beam bypassing the plasma and a second beam passing through the plasma. The plasma density can be obtained because of the proportionality with the phase speed of the electromagnetic waves in the plasma. By comparing at the phase shift of the two beams, the line integrated density is recovered. Local density variations can result in incorrect counts, which can be fixed by comparing the data to other diagnostics.

ASDEX Upgrade has five lines of sight for a deuterium cyanide nitrogen (DCN) laser interferometer, which operates at a wavelength of 195 μm. The information we get can be considered valuable, even if what we effectively compute is a line integrated quantity and not a local measurement.

3.1.3 Measurements of T_e

Electron Cyclotron Emission

The electron temperature is measured by radiometry of electron cyclotron emission (ECE) from a hot fusion plasma [18]. The ECE is the diagnostic usually providing the most accurate evaluation of the T_e on AUG, but only for large enough plasma densities, which make it not reliable at the edge of the plasma. Due to cyclotron radiation, hot electrons gyrate around the field lines; the cyclotron frequency is $\omega = \frac{eB}{m_e}$, where ω denotes the angular velocity, B the magnetic field and m_e the electron mass. The plasma typically emits like a blackbody source at the second harmonic of the electron cyclotron frequency. If the plasma is optically thick, the absolute intensity of the second harmonic X mode emission can be used to calculate the T_e and the Rayleigh-Jeans law of thermal emission applies:

$$T_e = \frac{8\pi^3 c^2}{k_B \omega^2} I \tag{3.1}$$

with I the intensity of the black-body radiation.

Because the magnetic field is radius dependent, the power spectrum displays a radial T_e profile.

AUG is equipped with a one-dimensional ECE heterodyne radiometer operating at frequencies between 89 GHz and 187 GHz, corresponding to magnetic fields from 1.6 T to 3.4 T. The radiometer has 60 channels, sampled at 1 MHz rate on different consecutive frequency bands; this allows the measurements of the electron temperature with a high spatial and temporal resolution. Due to calibration uncertainty, limited amplifier stability, non-linearity, and other difficulties, the absolute temperature measurement accuracy is predicted to be around 7%. The uncertainties can be minimized by utilizing ray tracing and a newly constructed model for the position of the warm resonances.

3.1.4 Measurements of T, n and rotation of light nuclei

Charge Exchange Recombination Spectroscopy

The charge exchange recombination spectroscopy (CXRS) system, based on the charge exchange processes between neutral atoms D^0 injected and ions of impurities I^{Z+} present in the plasma, measures the temperature, but also the rotation and the density of light impurities. Also CXRS is considered as an active radiation measurement.
The electron trapped by the impurity remains excited for a short period before experiencing radiative decay, resulting in a cascade of transitions to the ground level. The light emitted during specific transitions is studied spectroscopically and the Doppler shift and broadening of the recorded spectral line can be used to calculate the impurity velocity and temperature with the corresponding statistical uncertainty. The temperature of the impurities can be considered to be equivalent to that of the primary ions due to significant energy exchange generated by collisions.
This assumption may not hold when dealing with low density, high power discharges, where ion-impurity temperature variations can exceed 10%. Because it is a function of the main ion temperature, this can have a not necessarily negligible effect on the estimation of fusion reaction rates, but it is normally minimal.

On AUG, many CXRS systems are placed, probing both the core and the border of the plasma and monitoring toroidal and poloidal rotation with different lines of sight.

3.2 Profile fitting tools

This section provides the description of the two techniques applied, the Integrated Data Analysis (IDA) and AUGPED, in order to get the profile fittings of interest for each discharge analysed. These were then used as a starting point for the writing of a script capable of producing a pedestal stability analysis for each discharge analysed through a stability diagram.

3.2.1 Integrated Data Analysis

The Integrated Data Analysis (IDA) [24], [25] is a computational tool based on a Bayesian probability[12] method which yields profiles of electron temperature and density with an estimation of the respective statistical uncertainties.
A uniform way of combining data pertinent to fusion experimentation is provided by IDA. As a result, IDA deals with common problems that come up in fusion data processing. In IDA, all data is uniformly expressed as probability density functions that quantify analysis uncertainties applying Bayesian probability theory. IDA provides combined error distributions for a series of diagnostics, enabling comparison and integration of results from several diagnostics. Model comparison approaches can be used to validate physics models. Applications for typical data analysis benefit from IDA's non-linear error propagation, systematic effects inclusion, and comparison with multiple physics models capabilities. Applications include assessing models, background discrimination, outlier detection, and diagnostics design.

This approach makes use of several of the diagnostics outlined in the previous sections, including Thomson scattering, interferometer, lithium beam and the ECE. All the measured data is then mapped to the normalized poloidal flux coordinate ρ_{pol}.
The IDA procedure combines forward models for these multiple diagnostics to compute the probability distribution taking uncertainties and priors, such as smoothness, monotonicity, non-negativity restrictions.

The IDA profiles are being investigated automatically following each AUG discharge. The experimental activities and their analysis are substantially accelerated by the availability of a quick and reliable analysis of T_e and n_e. Furthermore, IDA offers additional information relevant to this investigation that aids in lowering the uncertainty associated with predicting the plasma kinetic quantities. This method also provides an accurate evaluation of core profile gradients.

3.2.2 AUGPED

AUGPED is an IDL based program whose purpose is of determining the pedestal properties. The experimental pedestal parameters, such as pressure, density, temperature, were evaluated through the employment of the AUGPED, where the different diagnostics can be aligned manually, differently from IDA where where everything is performed automatically. For this reason, an attempt was made to make fits more accurate and robust, that follow the trend of the data as closely as possible, in order to avoid substantial errors when fitting pedestal profiles; this could indeed later affect the pedestal stability analysis.

The fitting tools available in AUGPED do not take into account of the measurements errors.

[12] In the Bayesian method the course of actions in data analysis results in:

- a clear statement of the data analysis problem, giving importance to the forward calculation from the quantity of interest to the data and the background information. ;
- formulation of a data model with a quantification of all uncertainties;
- quantification of the prior information;
- the application of Bayes theorem, the inference step;
- the marginalization onto the quantity of interest, the focusing step.

Like IDA, also AUGPED is a code allowing users to combine the measurements from different diagnostics. Afterwards, these measurements can be processed to obtain fits of the main plasma kinetic quantities. Everything is mediated by a graphic user interface (GUI).

Due to the steep gradients in the pedestal region, the measurements of the various diagnostics are typically not naturally aligned to one another. Investigations are currently being conducted to determine the cause, although no clear causes have been identified.

Let us consider, as an example, a specific AUG discharge #33616 in fig. 3.2.

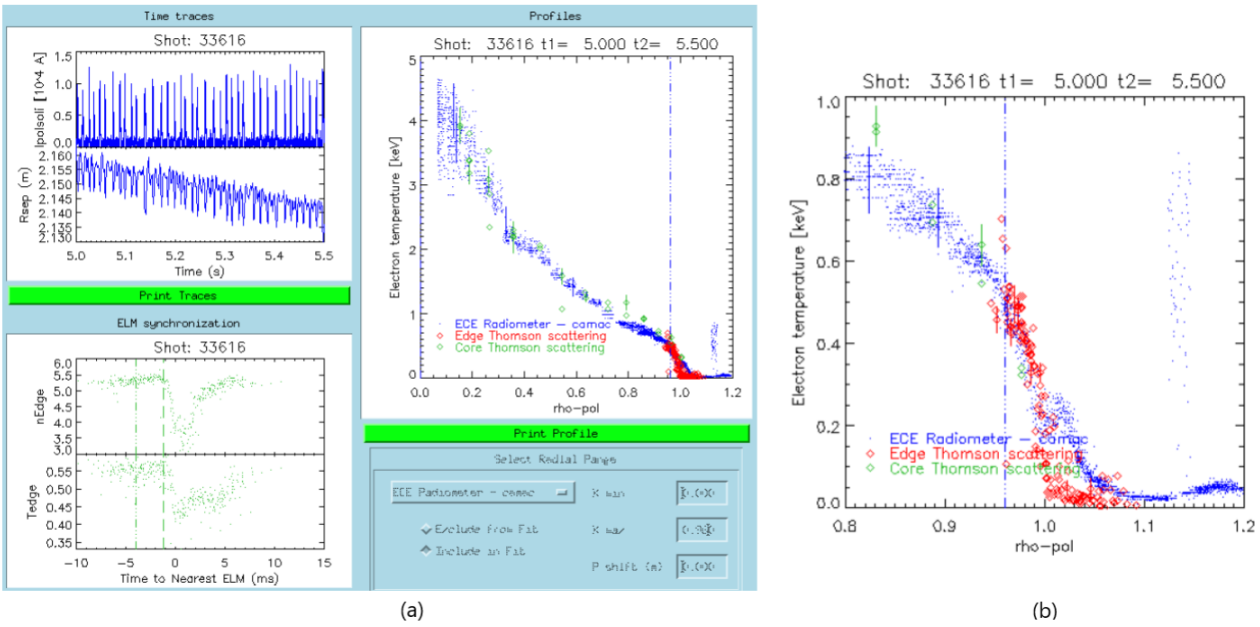

Figure 3.2: In (a), a screenshot of the AUGPED GUI, which allows to combine the measurements from different diagnostics, here for T_e, map them to the preferred radial coordinate, filter the data relative to ELMs and align the profiles to each other. In (b), the edge Thomson scattering data is shifted such that the separatrix T_e is $\approx$ 100 eV, and the other diagnostics are aligned to it.
The ECE data is discarded in the pedestal region, $\rho_{pol} > 0.96$ [14].

We are dealing with an approximately stationary phase, in this case between 5 and 5.5 seconds. The left hand side of the picture refers to the T_e data obtained by combining the ECE (blue), the core (green) and edge (red) Thomson scattering systems (3.2 (a)). The diagnostics chosen may vary from case to case according to the available data.
The data is then mapped on ρ_{pol}, also a time filter is applied to remove the time points corresponding to the ELM crashes and the ELM recovery phases, retaining only the steady-state phases prior to the ELM crash.
Since, as already explained, at low density the plasma is not optically thick and the ECE measurements are not reliable, zooming on the pedestal region, in 3.2 (b) we can see a a vertical blue line indicating that the ECE data outside of $\rho_{pol} > 0.96$ is discarded.

To solve the problem of the alignment of the diagnostics, the T_e measured by the edge TS is shifted such that the separatrix T_e is $\approx$ 100 eV (typical of AUG).
Then, the edge TS is aligned with all the other diagnostics. Since both the electron temperature and density are measured by this diagnostic, the shift in the density profile is equal to the temperature shift. The lithium beam is aligned to the TS density profile. The CXRS diagnostic's alignment is a more sensitive operation since there isn't a typical T_i value at the separatrix and because the diagnostic's readings have greater measurement uncertainties near the plasma's edge (particularly at the separatrix). As a result, the CXRS data is often fitted without any radial shifting.

In the end, we obtain fits (magenta lines) for the electron temperature, electron density and ion temperature as in 3.4. All these fits, for the pedestal region, are obtained using a specific function, the modified hyperbolic tangent function (mtanh) [26], [27], while for the core and SOL, usually second or third order polynomials are used, depending on the specific situation.

The mtanh function and its predecessor, which are called the tanhfit for convenience, were developed for the analysis of the H-mode transport barrier. The hyperbolic tangent happens to fit the form of the pedestal, the mtahh adds an additional degree of freedom to break the symmetry of the function.

The tanhfit fits typical edge H-mode profiles very well and the fit parameters are used to quantify the height, width and maximum gradient of transport barriers in edge density, temperature or pressure profiles. A linear term is added to the tanh to provide a good connection to the core profiles. This function had a discontinuity in the first derivative at the joint between the linear and tanh terms. A slightly modified function, called the mtanh, has been implemented which has a continuous first spatial derivative while providing almost exactly the same fit as the original function. The mtanh has been implemented by expanding the tanh function in terms of its exponentials and then multiplying the appropriate exponential by $(1 + \alpha z)$, where α is a constant which allows for a linearly rising profile in the core (figure 3.3).

The pedestal top measurements are accurately reproduced by this function fit. The fit of the electron density also reproduces well the integral measurements of the interferometer, illustrated by the overlap between the magenta crosses (fit) the cyan dots (measurements).

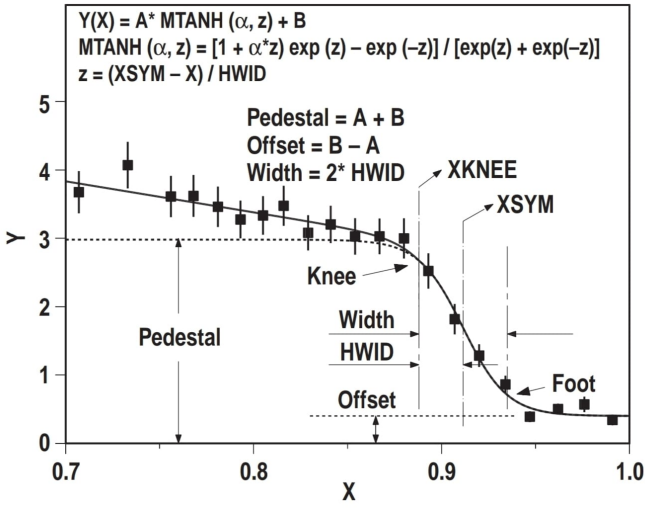

Figure 3.3: Modified tanhfit function, which is a fit to (X,Y) pairs where Y is a quantity, normally exhibiting a transport barrier, function of a spatial coordinate X. The fit parameters of the function are the location of the centre of the barrier (XSYM), the half-width of the barrier (HWID); the height of the top of the barrier (pedestal), the offset of the barrier and a parameter α which allows a smooth transition to a linear fit to the core profile.
This function has continuous first derivatives [26].

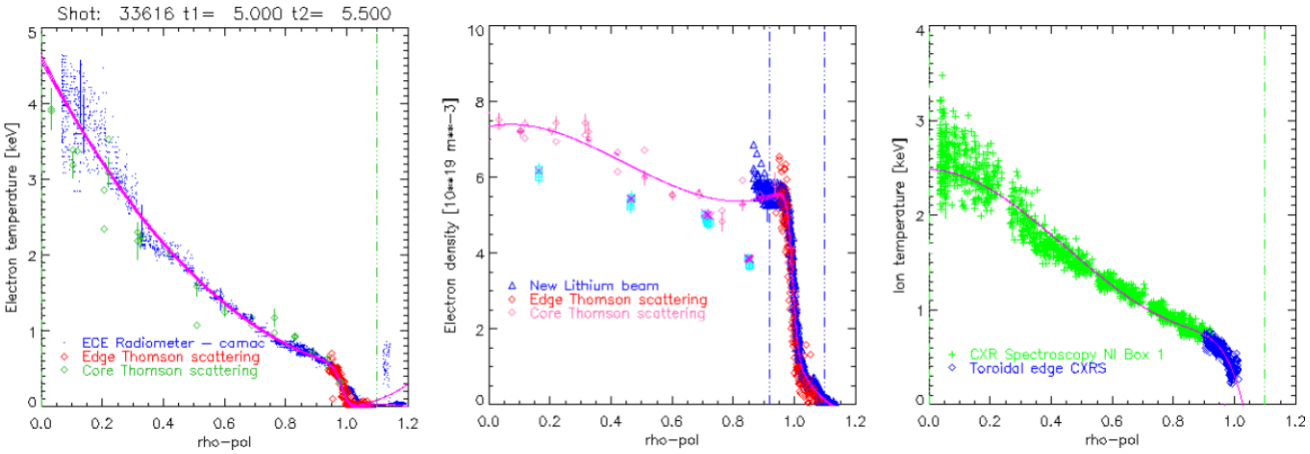

Figure 3.4: Resulting fits (magenta lines) of T_e, n_e and T_i thanks to the use of the modified hyperbolic tangent function. [14].

It is specified that, the core density gradient evaluated with AUGPED is not very reliable, because of the low radial resolution of the core TS diagnostic and its low accuracy in the pedestal top region. IDA also uses core TS and represents the uncertainty much better, but it doesn't have more information.

3.3 Equilibrium and stability

HELENA

The pressure and current density profiles corresponding to the different values of the pedestal width are passed to the HELENA (Hermite ELements Equilibrium solver for Normal-mode Analysis) [28], [29] high resolution equilibrium solver, written in the Fortran programming language, for a finer calculation of the equilibrium. The HELENA code is used to calculate the GS equation for a toroidal axisymmetric plasma with the use of isoparametric bicubic Hermite finite elements and fixed boundary for the equilibrium flux surfaces.

Let us see how the code works in more detail through its essential steps.

Firstly, the GS equation needs to be normalised with the use of three scaling parameters: the minor radius of the plasma boundary a (scale length), the vacuum magnetic field B_0 at R_0 (centre) and the total poloidal flux per radian at the plasma boundary ψ_1.

These scaling parameters are used to normalise the pressure gradient, the diamagnetic profile F, the toroidal current density and the total plasma current, all these are in of function of ψ. Furthermore, the coordinates of the plasma boundary, initially given in (R, z) are normalised to the length scale a as $x = \frac{R-R_0}{a}$, $y = \frac{z}{a}$ and $\epsilon = \frac{a}{R_0}$. The dimensionless GS equation follows:

$$\Delta\psi = -\frac{1}{\epsilon}(1+\epsilon x)^2 p'(\psi) - \frac{1}{\epsilon}F(\psi)F'(\psi) = -\frac{1}{\epsilon}(1+\epsilon x) j_{tor} \tag{3.2}$$

Afterwards, a second normalisation needs to be applied, done by defining unit profiles that are equal to 1 at the magnetic axis, $\Pi(\tilde{\psi}=0) = \Gamma(\tilde{\psi}) = J(\tilde{\psi}=0) = 1$ and the quantities that determine the amplitudes are noted as A, B and C. The flux surface averaged equation results as:

$$A\left(\left\langle \frac{1}{1+\epsilon x}\right\rangle \Gamma(\psi) + B\left\langle \frac{x(1+\epsilon x/2}{1+\epsilon x}\right\rangle \Pi(\psi)\right) = ACJ(\psi) \tag{3.3}$$

The usual input for HELENA is the quantity B, which represents $\frac{p}{FF'}$ and can be chosen freely. The condition that the normalised plasma flux $\psi = 1$ at the plasma boundary determines A and the total plasma current that is given by adjusting the global parameters, the input plasma current determines C.

The problem is then split into finite elements. In each element, a coordinate system (s, θ, ϕ) is locally formulated by defining θ in such way, that the field lines appear straight. A function is approximated with the bicubic Hermite element interpolating functions so that it is continuous inside the element boundaries.

Practically, this works as follows: a combination of two out of four input profiles are necessary, that is the safety factor q, $< j_{tor} >$, F ∇F or ∇p.

Being a fixed boundary solver, additionally to the previously listed inputs, HELENA needs a predefined LCFS, that lies inside the separatrix and defines the computational domain. As an initial guess, HELENA produces a set of nested flux surfaces that are just down-scaled plasma boundaries. The code then iteratively solves the GS equation until the convergence to a sufficiently accurate flux surface grid is achieved.

Besides equilibria, HELENA produces a wide range of output. The most relevant output in this analysis is the marginal ballooning stability.

MISHKA

MISHKA [30] is a linear ideal MHD code for stability analysis calculations, which scans a range of possible finite toroidal mode number. Going into detail, both ideal and resistive instabilities have an infinite spectrum of normal modes. In the simple case of a circular plasma with large aspect ratio (cylindrical approximation) these modes depend on the poloidal and toroidal angles as $e^{i(m\theta+n\phi)}$, where m and n are integer numbers called poloidal and toroidal wavenumber.

MISHKA is used to calculate the peeling-ballooning stability of the pedestal taking as input the pressure, the current density and the magnetic flux profiles and the geometry of the LCFS. Instead of using the energy principle, an eigenvalue equation is solved, yielding a growth rate γ and a mode structure of the perturbation.

The stability of each of the equilibria coming from HELENA is tested using the MISHKA code.

3.4 Workflow

So far, the tools and codes needed to implement a code in Python that can output stability diagrams of the pedestal region have been described. The code can be run thanks to the large number of computing resources available on the TOK cluster of the Max-Planck-Institute for Plasmaphysics (IPP).

In order, the code receives as input:

1. the AUG source, which can be ether IDA or AUGPED;
2. the discharge number to analyse;
3. a certain time range to verify corresponding to a stability phase of the plasma for to the specific discharge number in consideration (how to select these time intervals is explained in chap.4);
4. in the case of AUGPED, the edition of the discharge file to study can also be selected.

Next, the analysis of the available data begins.

The workflow is depicted in the diagram 3.5.

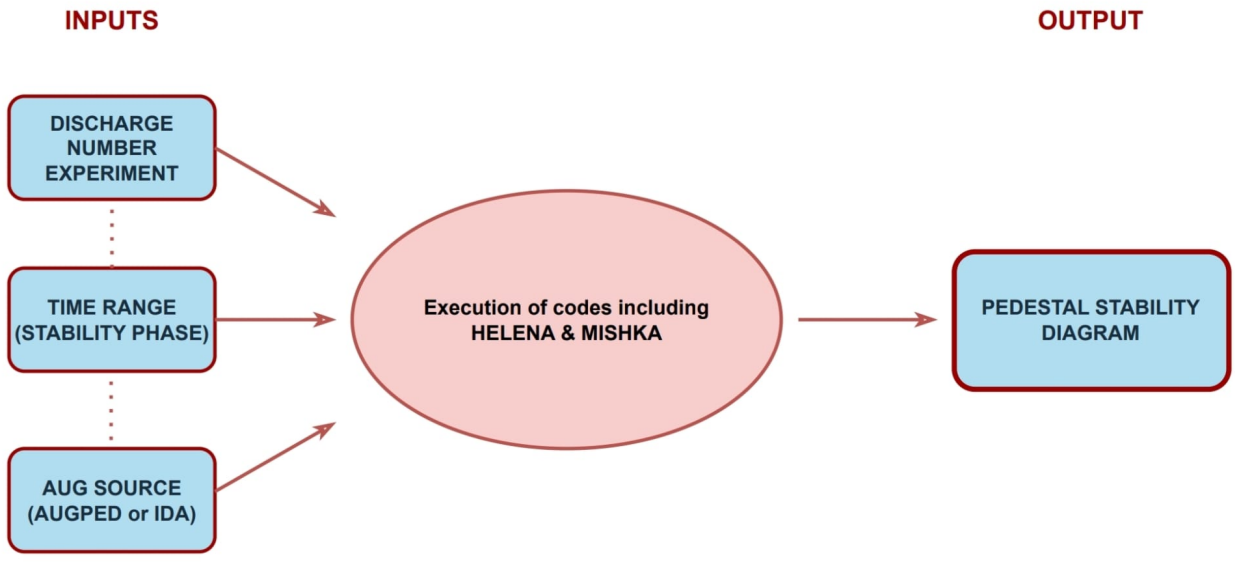

Figure 3.5: Workflow of the pedestal stability analysis.

Programs written in different programming languages, such as IDL and Python are employed.

Both HELENA and MISHKA are utilised in the process; equilibria are created with HELENA while the stability calculation are performed by MISHKA.

The total time to execute the code usually varies from 60 to 90 minutes depending on the discharge cases studied. This time mainly depends on the use of the equilibrium and stability codes.

Once the automation of the workflow is implemented it is applied to a database of experimental data from the ASDEX Upgrade tokamak to study the properties of the pedestal.

In the end, the inputs to plot the stability graphs related to the pedestal area are obtained.
These are shown and explained in detail in the subsequent chapter.

Chapter 4

Stability analysis

In the fourth chapter, the code for the stability analysis at various discharge number experiments is run, taking into account two types of plasma with different mass (different isotopes), one composed of deuterium and one of helium. In this way, an attempt is made to examine the behaviour of the plasma in the pedestal region depending on the isotope and mass with reference to the source AUGPED or IDA. The final results and distance of the operational point from the stability boundary, can vary from case to case and are shown in the stability diagrams in the ELM-free regimes.

4.1 Selection of the time interval

Once the stability workflow is implemented it is applied to a database of experimental data from the AUG tokamak to study the properties of the pedestal.
Four discharges composed of deuterium plasma attributable to experiments on AUG in June 2021 and five composed of helium plasma attributable to experiments in July 2022 are selected.

Discharges #39429, #39433, #39447 and #39454 are analysed for D plasma (table 4.1).

	$Time\,interval\,(s)$	$AUGPED$	IDA
#39429	4.25 - 4.55	✓	✓
#39433	6.05 - 6.35	✓	✓
#39447	4.25 - 4.55	✓	X
#39454	5.25 - 5.55	✓	✓

Table 4.1: Discharges, time intervals and AUG sources employed for D plasma.

Discharges #41453 and #41454, evaluated at different time intervals, are analysed for He plasma (table 4.2).

	$Time\,interval\,(s)$	$AUGPED$	IDA
#41453	5.65 - 5.90	✓	X
#41453	6.45 - 6.75	✓	✓
#41453	7.10 - 7.40	✓	X
#41454	5.85 - 6.10	✓	X
#41454	6.15 - 6.40	✓	X

Table 4.2: Discharges, time intervals and AUG sources employed for He plasma.

It is specified that for most of the experiments with helium plasma, only AUGPED was used as AUG source, was not available for data analysis; there is only one exception, as shown in table 4.2.

All these discharges have long enough time intervals for averaging of the profiles normally around 300 ms. This time range represents a stationary phase of the plasma where it has stopped evolving. This normally allows sufficient data to be analysed.

The parameters that must be constant during this stationary phase are fuelling rates, density, temperature, heating power and stored energy.
Concerning the heating power, in order to increase the plasma temperature to the value required to produce a large enough number of fusion reactions and to keep it to that value, a method is required to heat the plasma and to balance the losses due to the imperfect confinement.

Three main categories for plasma heating are listed below:

- ohmic heating, in order to achieve a rotational transform of the magnetic field, a current is induced in the plasma. This current has the side effect of heating the plasma by Joule effect. This ohmic heating is however not sufficient to bring a tokamak to the temperature required for fusion. That is why we need to add other heating methods;

- neutral beam injection (NBI), the introduction of particle beams into the plasma requires that the particles are electrically neutral, because otherwise they would be deflected by the tokamak magnetic field. These energetic neutral atoms are then ionized by collisions with the plasma particles: at that point, they are confined by the magnetic field, and gradually release their energy to the plasma through further collisions, thermalising. It is desirable that the power deposition takes place preferentially in the plasma core, and this can be obtained by adjusting the beam energy;

- Wave heating, which is the heating by injection of electromagnetic waves at radiofrequency or in the microwave range In order to achieve it effectively, it is required that the injected radiation can propagate, without being reflected, up to a plasma region where a resonance condition causes its absorption, transferring its energy to the plasma particles. The variety of waves which can propagate in a magnetized plasma allows different wave heating schemes. For all of them the same basic setup is required: a high power generator located far from the plasma, a transmission line with low losses, and an antenna coupling effectively the wave to the plasma.
  Without entering into the details of the phyisics of wave propagation in a magnetized plasma, which is quite complex, especially when the medium inhomogeneity is taken into account, we can mention the three schemes which have turned out to be the most appropriate: the ion cyclotron resonance heating (ICRH); lower hybrid resonance heating (LH) and electron cyclotron resonance heating (ECRH).

In AUG, there are three methods of plasma heating: NBI, ECRH and ICRH.
For the purpose of our study, only the first two methods were effectively applied.

The highest heating powers are delivered by the NBI.

4.2 Role of isotope mass

The isotopic mass is a key element that must be taken into account for the stability analysis, it may lead to very different results.

Experiments studying H-mode confinement and different ion masses on AUG and JET show that a strong isotope mass dependence in the pedestal or plasma edge is found which is enhanced at high gas puffing[13] [32]. This happens because, given similar engineering parameters, the ELM type varies while moving from D to H. This is probably owing to variations in the inter-ELM transfer with isotope mass. For example, when technical parameters like power, gas, and plasma form are identical, the pedestal density is lower in H even if temperatures may be same, leading to lower pressure. To comprehend the root of this disparity, it is crucial to take into account three key factors: ELM stability, ELM losses, and inter-ELM transport.
The least understood of the three hypotheses to explain the isotope dependency in the pedestal is the inter-ELM transport. Although there is ongoing research on the theoretical aspects of heat and particle transport in the H-mode pedestal, the high gradients make it challenging to simulate; nevertheless, this is changing at the moment.

It is probable that collisional drift waves play a significant role in H-mode. Drift waves were discovered in the edge of L-mode plasmas and exhibit characteristics that explain the reported mass dependence of transport. Even though interpretative experimental research frequently discover that the transport in H is greater than in D, these studies' uncertainties are very considerable. Particularly, a trade-off between matching the sources and matching the profiles must be made because of the pedestal's mass dependence.

Due to the challenge of applying numerical codes in the pedestal region, it is difficult to differentiate between an impact caused by the source (profile rigidity, electron-ion equipartition, etc.) and an impact caused by changing profiles (collisionality, T_i/T_e, etc).

By changing only the triangularity and leaving the other machine parameters unchanged, the pedestal may be made to match those in H and D plasmas.

Plasma shaping [34], [35] is an is an influential contribution to the study of the pedestal. Referring to the shape of the poloidal cross section of the LCFS or separatrix of a tokamak, two parameters are distinguished:

- the triangularity (δ), especially the triangularity opposite the dominant X-point, the upper triangularity for a lower null plasma, which influences the stability of the pedestal and ELMs. The overall δ (considering upper and lower contributions of δ), is the horizontal distance between the plasma geometric major radius R and the X point (normalised to the minor radius);

- The ellipticity (also elongation) refers to $\kappa = \frac{b}{a}$ where b is the height of the plasma measured from the equatorial plane and a is the plasma minor radius. Higher elongation is beneficial for fusion performance, but comes with increased vertical instability growth rate and thus increased risk of vertical displacement event type disruptions. Because of vertical stability constraints, $\kappa \approx 1.8$.

Other contributions that can affect the stability of the pedestal are: the density, β_{pol}, the position of the density profile and Z_{eff} [14], which takes into account the dilution of the main ions caused by impurity atoms. The dominant AUG relevant impurities in D and He plasma are given by Boron (B), Carbon (C), Nitrogen (N) and Neon (Ne).

[13] A gas puff in plasma physics is a controlled injection of gas into a plasma for various purposes, including diagnostic measurements, plasma control and fuelling in fusion research.

[14] The effective nuclear charge is the actual amount of positive (nuclear) charge experienced by an electron in a multi-electron atom. The term *effective* is used because the shielding effect of negatively charged electrons prevent higher energy electrons from experiencing the full nuclear charge of the nucleus due to the repelling effect of inner layer.

The effect of a high density area located in the high-field side scrape-off layer (HFS SOL) on plasma confinement has been demonstrated by experimental data [38]. It has been proven that increasing main ion fueling raises the density of the separatrix and moves the density profile outward. The achievable pedestal top pressure is predicted to reduce by 25% as a result of this shift, which is consistent with experimental findings from the gas scan.
Nitrogen (N) seeding can be used to reduce the high-field-side high-density front (HFSHD). With seeding, especially at high heating powers, significant increases in the feasible pedestal top pressure are seen. These gains are connected with inwardly shifted density profiles, a decrease in the HFSHD and a drop in separatrix density. The impact of a radially changed pressure profile on PB stability is further supported by interpretive linear stability analysis, with an inward shift enabling access to higher pressure gradients and pedestal widths.

Further studies on JET [37] show a reduction of the pedestal pressure with increasing separatrix density over pedestal density (n_e^{sep}/n_e^{ped}).
There are two different mechanisms at work in the correlation. The pedestal pressure is shifted radially outwards by an increase in n_e^{sep}/n_e^{ped} up to ≈ 0.4, which also lowers the pressure height and degrades the peeling-ballooning (PB) stability. Above a value of about 0.4, the position's influence reaches saturation. The decrease in pedestal pressure for larger values is attributed to enhanced turbulent transport and most likely, resistive MHD effects. The resistivity η_e and the pedestal turbulent transport rise when the increase over 0.4 decreases $\nabla n_e/n_e$. The pedestal resistivity rises as a result of the decreased pressure gradient and pedestal temperature. Increased resistivity may cause resistive ballooning modes to become unstable, thus decreasing pedestal stability.

4.3 Stability diagrams

The stability diagrams are 2D surface plots (also called contour plots) of three-dimensional data. Next to the diagram, a colour bar helps the visualization, it is a graphical representation used in visualizations to interpret the colours used in a plot. It provides a scale that maps the numerical values in a dataset to colours. In other words, it shows the correspondence between the data values and the colours displayed in a plot.

The resulting stability graphs are obtained identifying:

- the maximum edge current density averaged over the flux surfaces, $< j_{max} >$ (MA/m^2). This is dependent from the ohmic and the bootstrap current which is a Neoclassical [15] toroidal current produced in the presence of a pressure gradient, associated with the existence of trapped (banana) particles in toroidal magnetic confinement systems. A requirement for the existence of the bootstrap current is its inverse dependence on collisionality. The difference in particle density on banana orbits crossing a given radial position r leads to a net toroidal current at r.

  The bootstrap current [6] is roughly estimated as:

$$j_b = -\epsilon^{1/2} {B_P}^{-1} \frac{dp}{dr} \tag{4.1}$$

  where ϵ is the inverse aspect ratio a/R and p the pressure.
  More precise estimates can be made by simulating particle orbits.

[15] The Neoclassical Transport Model provides a model for the transport of particles, momentum and heat due to Coulomb collisions in confined toroidal plasmas, assuming that the plasma is in a quiescent state. The difference between the Neoclassical and the Classical models lies in the incorporation of geometrical toroidal effects, which give rise to complex particle orbits and drifts that were ignored in the latter.

- the maximum normalised pressure gradient α_{max}, adimensional parameter, where α is defined as:

$$\alpha = -2\mu_0 \frac{\partial V}{\partial \psi} \frac{1}{4\pi^2} \left(\frac{V}{2\pi^2 R_0} \right)^2 \frac{\partial p}{\partial \psi} \approx -\frac{2\mu_0 R_0 q^2}{B^2} \frac{dp}{dr} \tag{4.2}$$

  with the magnetic field is mainly given by the toroidal contribution.
  The first alpha relation is general, as it is valid for any shaped plasma [31]; the second is to be applied to a cylindrical plasma [7] resulting more immediately comprehensible.

- the normalised growth rate: $\gamma \cdot \tau_{Alfvén}$.

  In plasma stability theory, the term growth rate γ refers to the rate at which certain instabilities or waves within a medium increase in amplitude over time. These instabilities can arise in plasma physics due to various factors such as temperature gradients, magnetic fields or the presence of different particle species within the plasma. The growth rate is a fundamental parameter used to understand the behaviour and stability of plasmas. γ is an output of the MISHKA code from the solution of the eigenvalue problem. Growth rates for MHD instabilities are expressed in units of inverse time.

  Alfvén time $\tau_{Alfvén}$ [7] is the time taken for an Alfvén wave[16] to travel one radian in the toroidal direction. This is a measure of the time-scale on which Alfvénic magnetohydrodynamic effects can occur.
  The Alfvén velocity is defined as:

$$v_{Alfvén} = \frac{B_0}{(\mu_0 \rho_0)^{1/2}} \tag{4.3}$$

  with B_0 and ρ_0 being the magnetic field and mass density respectively. The mass density is the sum over all species of charged plasma particles: $\rho = \sum_i n_i m_i$ with species density n_i and species mass m_i; for a D plasma: $\rho_D = 2 m_H n_D$ while for He: $\rho_{He} = m_{He} n_{He}$.
  $v_{Alfvén}$ is important for the dynamics of ideal MHD, it sets the natural timescale, the Alfvén timescale:

$$\tau_{Alfvén} = \frac{L}{v_{Alfvén}} \tag{4.4}$$

  Inserting typical parameters of magnetically confined fusion plasmas, $\tau_{Alfvén} \approx 1 - 10\ \mu s$, quite fast, because of the small mass of the very low density plasma. As a result, ideal MHD instabilities in tokamaks frequently grow too quickly to be controlled by magnetic feedback without the aid of passive features like conducting wall components.

The final diagrams are thus composed by the superimposition of :

- a contour plot relating to stability explained by the scale of colours: from blue (stable) to warm colours such as yellow/red (unstable). This is obtained from a matrix with $< j_{max} >$ and α_{max} as elements, obtained after running the stability script with MISHKA;

- the MHD stability boundary, which refers to the boundary or threshold conditions that separate stable plasma states from unstable ones. It is represented by a dashed black line delimiting the stable zone from the unstable one;

[16] Alfvén waves, discovered by Hannes Alfvén, are fundamental waves prevalent in magnetically confined plasmas existing in the nature and laboratories. Alfvén waves play important roles in the heating, stability, and transport of magnetized plasmas.

- an operational point. It is important to highlight the distance from the stability boundary also considering the relative uncertainty of the measurement. An uncertainty on the measurement of approximately 15 % is given, for all the points. This is rough, but reasonable considering the uncertainty on radial resolution, temporal resolution, the diagnostic measurement, the source used to the fittings and the gradient measurement.

4.4 Deuterium plasma

Deuterium or heavy hydrogen is a natural isotope of hydrogen and its atomic nucleus consists of a proton and a neutron. Naturally occurring hydrogen contains a deuterium component of about 0.015 %. In the oceans, there are about 4.6×10^{13} tons of deuterium.

Deuterium occurs in trace amounts naturally as deuterium gas, but most of the naturally occurring deuterium atoms in the Universe are bonded with a typical H atom to form a gas called hydrogen deuteride. Similarly, natural water contains trace amounts of deuterated molecules, almost all as semiheavy water HDO with only one deuterium atom. This makes it an attractive fusion fuel from the perspective of fuel availability and safety. Also, it is considered relatively safe compared to tritium, which is radioactive, making it a preferred choice for many fusion research experiments. However, safety precautions are still essential when working with deuterium plasmas at high temperatures and pressures.

The nucleus of deuterium is called a deuteron. It has an approximate mass of 2.014 Da[17], just over 1.875 GeV while the charge radius of the deuteron is 2.128 fm = 2.128×10^{-15} m.

D plasmas are extremely hot, with temperatures ranging from millions to tens of millions of degrees. These high temperatures are required to overcome the electrostatic repulsion between positively charged nuclei and facilitate nuclear fusion. Fusion plasmas, including deuterium plasmas, need to have high particle densities to increase the likelihood of nuclear collisions and fusion reactions. A significant portion of deuterium atoms are ionized at fusion relevant temperatures losing electrons. This leads to the presence of deuterium ions (deuterons) and free electrons. Achieving and maintaining the necessary density and temperature is a significant challenge in fusion research.

For all the D plasma discharges under consideration, the pedestal top pressure is 7 kPa, relatively high.

Discharge #39429

A list of the mean values of the main parameters related to #39429 is shown in 4.3:

	B_ϕ (T)	I_p (MA)	n_e ($\times 10^{19}$ m^{-3})	q_{95}	P_{heat} (MW)	κ	δ_{upper}	δ_{lower}
#39429	-2.5	0.8	6.4	5.0	NBI: 6.7 EC: 2.1	1.73	0.11	0.50

Table 4.3: Main parameters for #39429.

[17]The dalton (Da) or unified atomic mass unit (u) is a non-SI unit of mass defined as 1/12 of the mass of an unbound neutral atom of carbon-12 in its nuclear and electronic ground state at rest. The atomic mass constant can also be expressed as its energy equivalent:

$$m_u c^2 = 1.49241808560(45) \times 10^{-10}\ J = 931.49410242(28)\ MeV \tag{4.5}$$

.

The negative sign of the toroidal magnetic field is due to $\nabla \mathbf{B} \times \mathbf{B}$, which should point downwards to the X-point for easier H-mode access. In the coordinate system of AUG, this implies a negative sign for the toroidal field (clockwise B_ϕ).

It is specified that δ_{lower} remains almost fixed in all plasmas considered here while δ_{upper} can change from experiment to experiment. The mean triangularity of #39429 is a low δ.

The *flattop* current phase of the plasma discharge, that is the period of time during the experiment in which the plasma is stable and has reached a relatively constant temperature and density, is 1.20 - 9.00 s.

The time interval 4.25 - 4.55 s taken into account for the analysis is justified by looking at the time-traces 4.1 for some of the main parameters, these bring to attention the stationary phases (in grey).

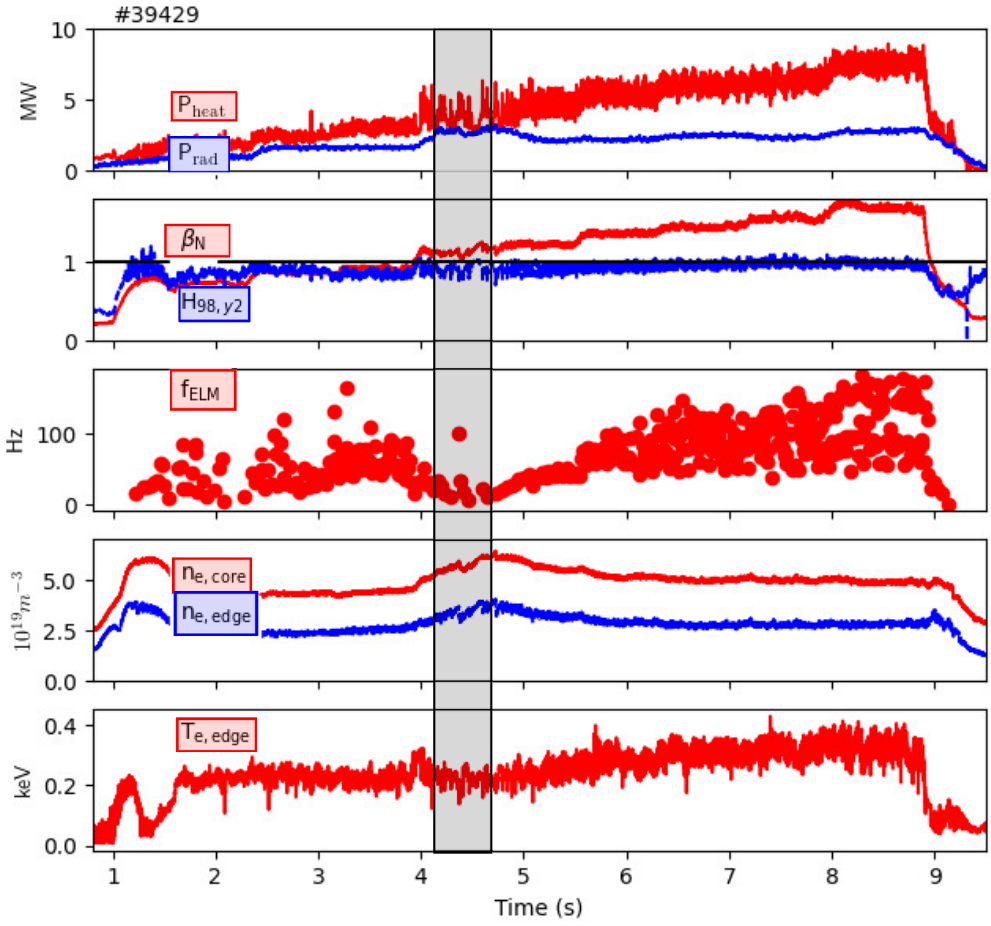

Figure 4.1: Time-traces for various parameters. The grey area highlights the approximately stationary phase (in the range 4.25 - 4.55 s) for some of different parameters considered for the discharge #39429. From the bottom we have represented in order: the electronic temperature at the edge $T_{e,edge}$ in keV; the electronic density at the core $n_{e,core}$ and edge $n_{e,edge}$ in $10^{19}m^{-3}$; the frequency of the ELMs f_{ELM} in Hz, the normalised beta factor β_N and H confinement factor H98(y,2) (from scaling laws); lastly the radial P_{rad} and heating power P_{heat} in MW.

Both β_N and the H factor H98(y,2) are adimensional parameters.

β_N is the normalised β factor (or Troyon factor) [6], an operational parameter indicating how close the plasma is to reaching destabilising major MHD activity. Its definition is:

$$\beta_N = \beta \frac{aB_\phi}{I_p} \tag{4.6}$$

where β is mainly given by the toroidal component, B_ϕ is the toroidal magnetic field, a the minor radius and I_p the plasma current.

The maximum value of the normalised β has been determined numerically by Troyon to be 0.028 [39]. This limit results from many different numerical studies determined to find the overall limit out of many different MHD instabilities, such as ballooning and kink mode. Empirical evaluation from the data of different tokamaks raises this value slightly to 3.5, although significantly higher values have been achieved.

The stability diagrams for #39429 are displayed in diagram 4.2 for AUGPED and in diagram 4.3 for IDA source.

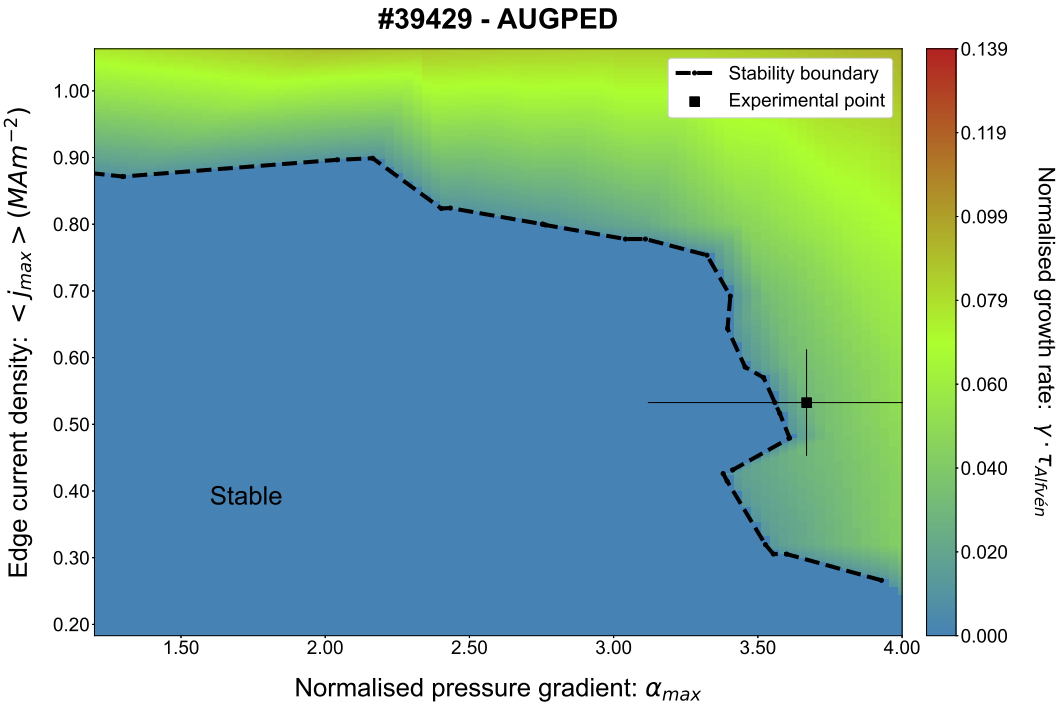

Figure 4.2: Stability diagram showing the position of the operational point (with errorbars) with respect to the stability boundary for #39429 in the time interval 5.25 - 5.55 s using AUGPED as source.

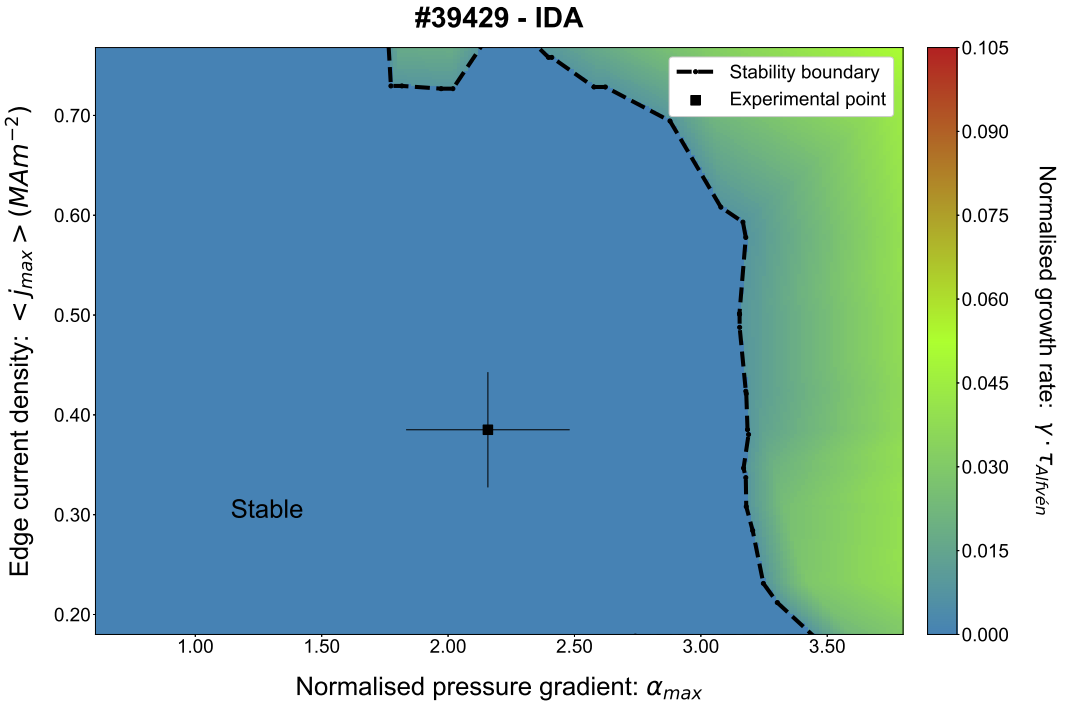

Figure 4.3: Stability diagram showing the position of the operational point (with errorbars) with respect to the stability boundary for #39429 in the time interval 5.25 - 5.55 s using IDA as source.

Comparing the two #39429 graphs, in diagram 4.2 the experimental point is close to the MHD stability boundary, even if not exactly on it, as we would expect. However, considering the uncertainty of 15% on the operational point, showed through the errorbars, it can be assumed to be almost on the boundary. Looking now at diagram 4.3, the operational point results fully stable, even within the error on the measurement.

Discharge #39433

A list of the main parameters related to #39433 is shown in table 4.4:

	B_ϕ (T)	I_p (MA)	n_e ($\times 10^{19}$ m^{-3})	q_{95}	P_{heat} (MW)	κ	δ_{upper}	δ_{lower}
#39433	-2.5	0.8	7.7	5.3	NBI: 6.7 EC: 1.4	1.74	0.25	0.48

Table 4.4: Main parameters for #39433.

The triangularity is a high δ.

The *flattop* phase is in the range 1.20 - 8.00 s.
The time interval taken into account is justified exactly in the same way as did for #39429; the related time-traces are therefore no longer reported.

The stability diagrams for #39433 are displayed in diagram 4.4 for AUGPED and in diagram 4.5 for IDA source.

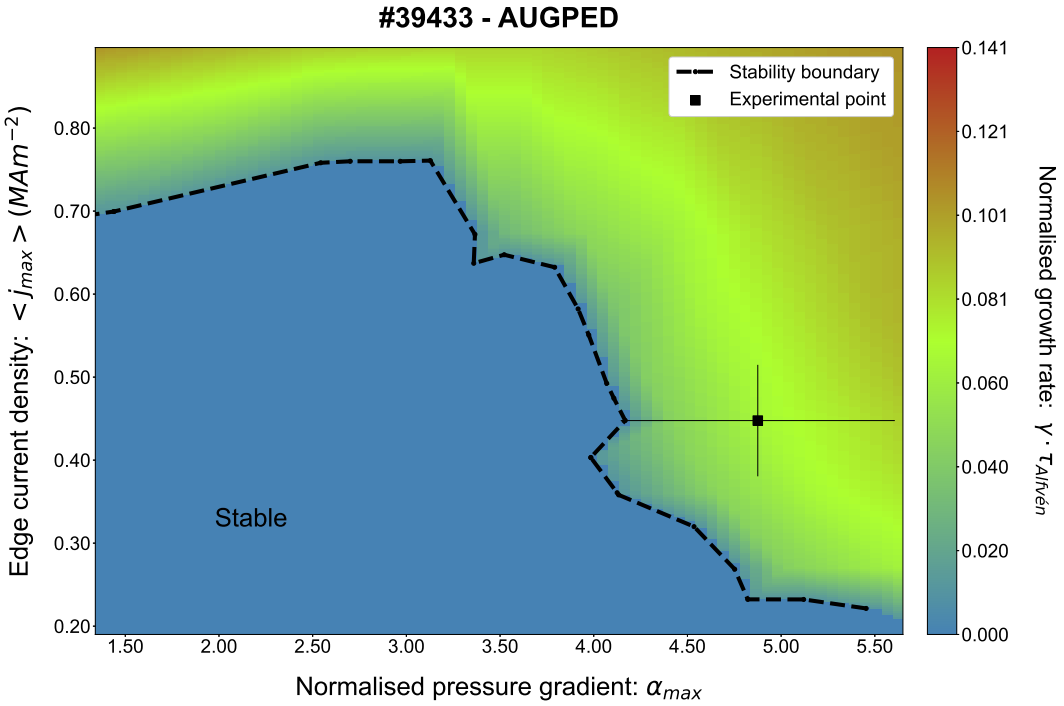

Figure 4.4: Stability diagram showing the position of the operational point (with errorbars) with respect to the stability boundary for #39433 in the time interval 6.05 - 6.35 s using AUGPED as source.

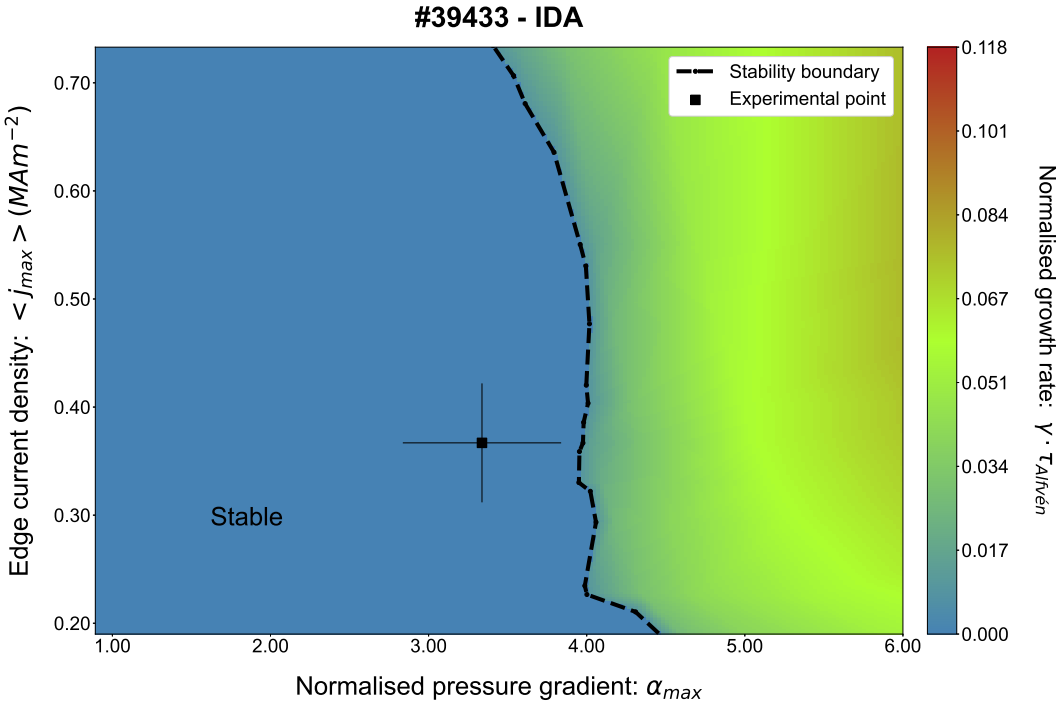

Figure 4.5: Stability diagram showing the position of the operational point (with errorbars) with respect to the stability boundary for #39433 in the time interval 6.05 - 6.35 s using IDA as source.

The same considerations as in #39429 apply to #39433.

Discharge #39447

A list of the main parameters related to #39447 is shown in table 4.5:

	B_ϕ (T)	I_p (MA)	n_e ($\times 10^{19}$ m^{-3})	q_{95}	P_{heat} (MW)	κ	δ_{upper}	δ_{lower}
#39447	-2.5 T	0.8	8.0	5.4	NBI: 4.4 EC: 1.3	1.73	0.25	0.46

Table 4.5: Main parameters for #39447.

The triangularity is a high δ.

The *flattop* phase here is 1.60 - 7.80 s.

The stability diagrams for #39447 are displayed in graph 4.6 for AUGPED while for IDA no good values were encountered, hence the IDA stability diagram is not relevant to the analysis.

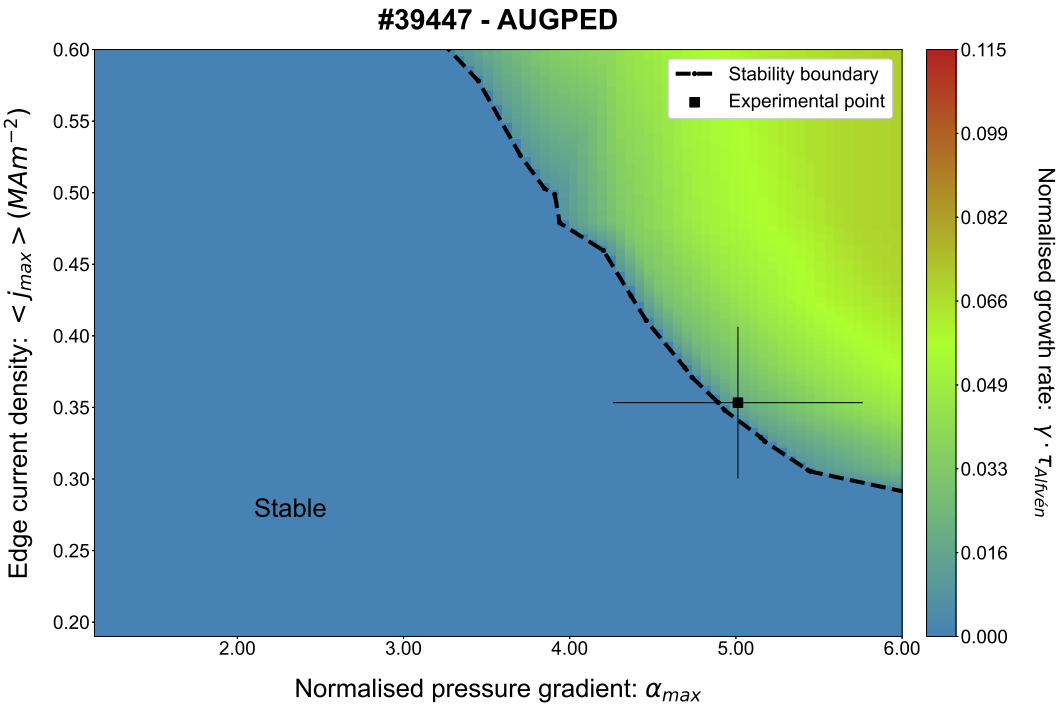

Figure 4.6: Stability diagram showing the position of the operational point (with errorbars) with respect to the stability boundary for #39447 in the time interval 4.25 - 4.55 s using AUGPED as source.

Discharge #39454

A list of the main parameters related to #39454 table is shown in 4.6:

	B_ϕ (T)	I_p (MA)	n_e ($\times 10^{19}$ m^{-3})	q_{95}	P_{heat} (MW)	κ	δ_{upper}	δ_{lower}
#39454	-2.5	0.8	7.1	5.1	NBI: 7.5 EC: 2.1	1.73	0.11	0.47

Table 4.6: Main parameters for #39454.

The triangularity is a low δ.

The *flattop* phase here is in the range 1.22 - 8.60 s.

The stability diagrams for #39447 are displayed in graph 4.7 for AUGPED and in graph 4.8 for IDA source.

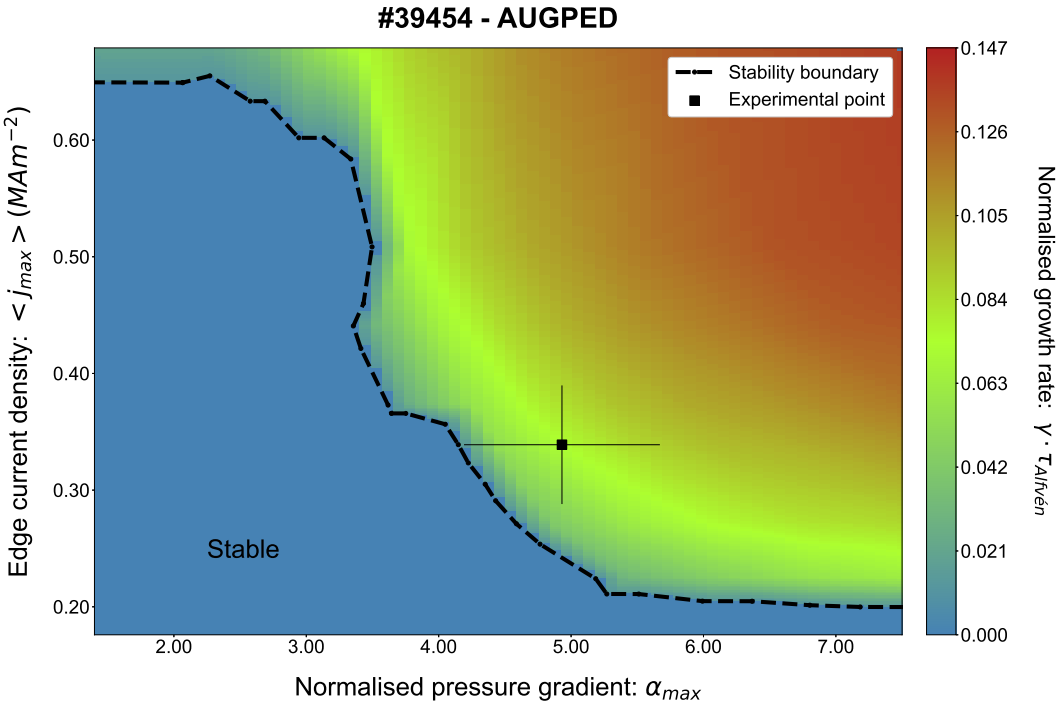

Figure 4.7: Stability diagram showing the position of the operational point (with errorbars) with respect to the stability boundary for #39454 in the time interval 5.25 - 5.55 s using AUGPED as source.

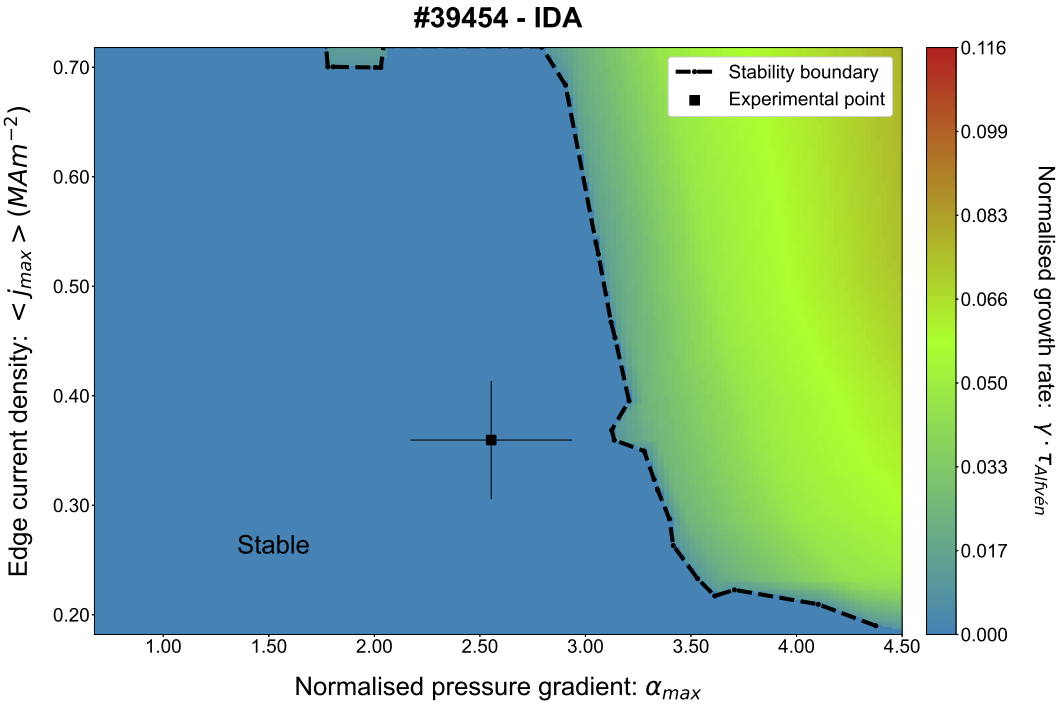

Figure 4.8: Stability diagram showing the position of the operational point (with errorbars) with respect to the stability boundary for #39454 in the time interval 5.25 - 5.55 s using IDA as source.

4.4.1 Discussion on D plasma

Studying the four cases examined, a common pattern can be found: IDA, being a default fitting, tends not to give correct results for the gradients, which tend always to be too low. On the other hand, considering the diagrams obtained by using AUGPED, tool for manual fittings, these turn out to have the operational point, within the limits of the 15 % uncertainty, on the stability boundary. In fact, if the pedestal is ideal peeling-ballooning limited, the point should lie on the stability boundary. A good example can be observed with the discharge #39447.

4.5 Helium plasma

Helium (He) is a chemical element with atomic number (Z) 2. It is a colourless, odourless, tasteless, non-toxic, inert, monatomic gas and the first in the noble gas group in the periodic table. It is the second lightest and second most abundant element in the observable universe, after H. It is present at about 24 % of the total elemental mass. Its main isotopes are He-3 and He-4 with respective abundances of 0.0002% and 99.9998 %. Its average atomic mass is approximately 4.003 Da.

Most terrestrial helium present today is created by the natural radioactive decay of heavy radioactive elements (as thorium and uranium), as the alpha particles emitted by such decays consist of helium-4 nuclei. This radiogenic helium is trapped with natural gas in concentrations as great as 7% by volume, from which it is extracted commercially by a low-temperature separation process called fractional distillation. Terrestrial helium is a non-renewable resource because once released into the atmosphere, it promptly escapes into space.

A helium plasma is a state of matter in which helium gas becomes ionized, resulting in a mixture of electrons, helium ions, and neutral helium atoms. Helium plasmas typically have lower plasma ion densities compared to plasmas containing deuterium and tritium. This property can affect the behaviour of the plasma and its interactions with the magnetic fields used for confinement.

It is chemically inert, meaning it does not readily react with other elements or itself. This inertness can be advantageous in maintaining a stable plasma environment for diagnostic purposes.

The ITER Research Plan states that helium (He) is a potential choice for the primary plasma species and a substitute for hydrogen (H) to achieve H-mode conditions without causing overly intense activation of vacuum vessel components during the initial non-nuclear phases of ITER. Additionally, helium will be produced in the plasmas of the following nuclear phases as a result of deuterium-tritium fusion events, at lower concentrations. In order to achieve these goals, the EUROfusion Tokamak Exploitation Task Force conducted experimental campaigns in He plasmas on the ASDEX Upgrade and JET tokamaks in 2022 to help ITER decide whether to carry out its non-nuclear operating phases using hydrogen or helium plasmas [40]. A two-week session in pure and mixed helium plasmas (D/He and H/He) was conducted in AUG. The usual ECRH and ICRH as well as NBI (Neutral Beam Injection) systems were used during the He operations for heating the plasma

Regarding AUG, considerable scenario development work was done in 2015 and 2019 during the previous helium campaigns. The foundation for further research was chosen from a set of reliable type-I ELMy H-mode situations, both with low and high δ and mostly employing 0.8 MA for the plasma current and 2.5 T for the toroidal field. The two heating techniques were compared with one another, as well as with the current H and D databases, using either NBI or ECRH.

There are significant findings for these He campaigns, in both AUG and JET:

- despite the fact that the LH threshold is lower in He than in H, the tests have shown that attaining the type-I ELMy regime is more difficult in He. The increased utility of employing He instead is debatable because high heating powers in both H and He are required for ITER to operate in the desired operational situations;

- On beryllium (Be) and tungsten (W) plasma-facing components (PFCs), different erosion and deposition patterns can be seen more obviously than in H plasmas. Only plasmas with a He concentration under 13% were capable of suppressing ELMs;

- there are not any significant changes in the pedestal properties of H, D, and He from the pedestal side, but the wall material has a significant impact. Even though the confinement of D and He is equivalent, some modifications to particle transport are anticipated;

- higher densities were required for the initiation of detachment and recycling was significantly reduced in He compared to D, possibly because He lacks the molecular channels necessary for separation;

- the persistence of helium impurities in H/D plasmas after the campaigns, together with poor He pumping by cryos, demonstrated that the requisite plasma purity is easier to achieve when moving from hydrogenic gases to He than the other way around.

The helium plasmas presented here were chosen to have a pedestal top pressure of 7 kPa to compare with the deuterium cases.

Discharge #41453

A list of the main parameters related to #41453 is shown in table 4.7:

	B_ϕ (T)	I_p (MA)	n_e ($\times 10^{19}$ m^{-3})	q_{95}	P_{heat} (MW)	κ	δ_{upper}	δ_{lower}
#41453	-2.5	0.8	8.1	5.1	NBI: 9.7 EC: 1.8	1.72	0.10	0.46

Table 4.7: Main parameters for #41453.

The triangularity is a low δ.

The *flattop* phase here is 1.00 - 8.00 s.

Three different time intervals have been taken into account for #41453, reported in the following subsections.

Time interval: 5.65 - 5.90 s

The stability diagram for #41453 in the time interval 5.65 - 5.90 s is displayed in graph 4.9 for AUGPED (IDA is not taken into consideration since no good points were available from the fitting).

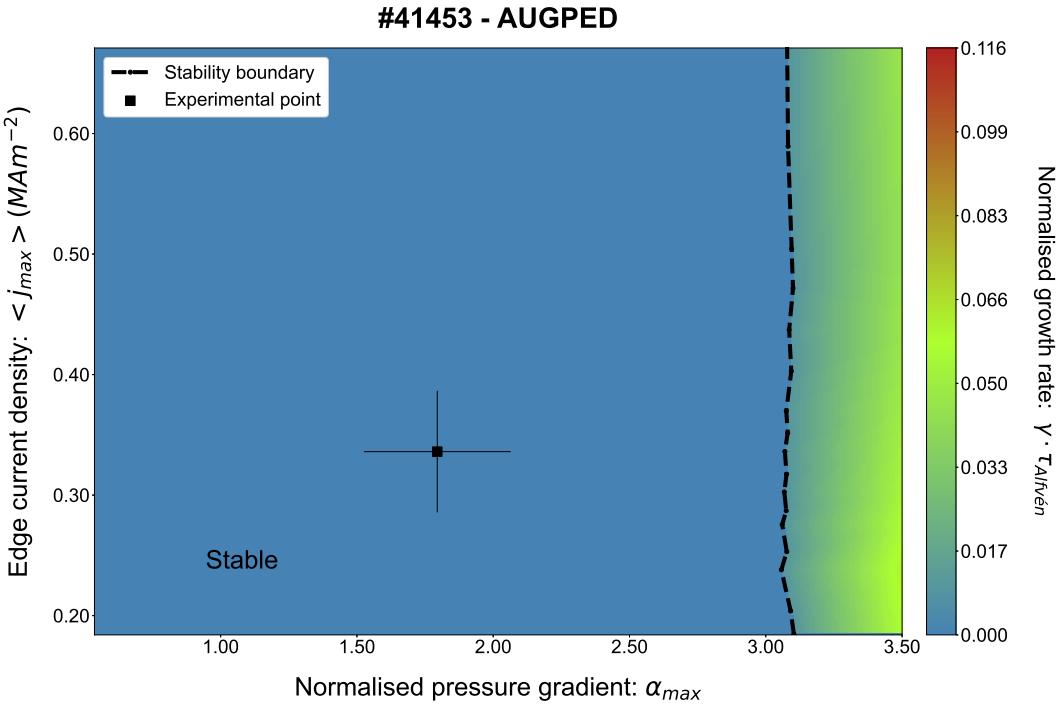

Figure 4.9: Stability diagram showing the position of the operational point (with errorbars) with respect to the stability boundary for #41453 in the time interval 5.65 - 5.90 s using AUGPED as source.

The operational point lies well within the boundary.

Time interval: 6.45 - 6.75 s

The stability diagrams for #41453 in the time interval 6.45 - 6.75 s are displayed in graph 4.10 for AUGPED and in graph 4.11 for IDA source.

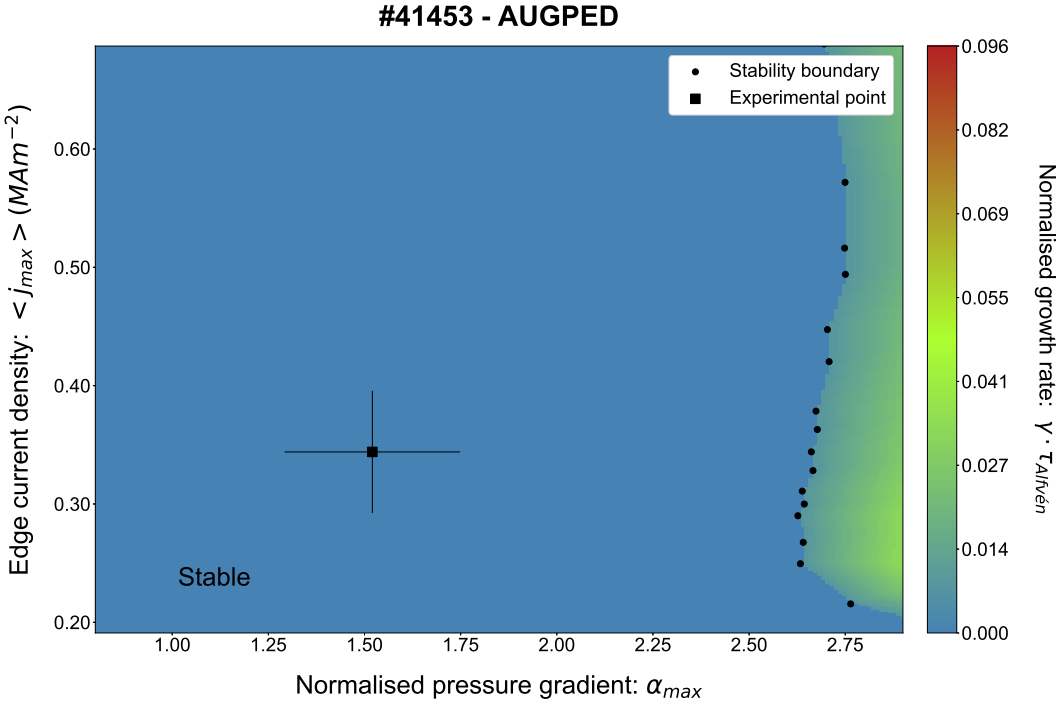

Figure 4.10: Stability diagram showing the position of the operational point (with errorbars) with respect to the stability boundary for #41453 in the time interval 6.45 - 6.75 s using AUGPED as source.

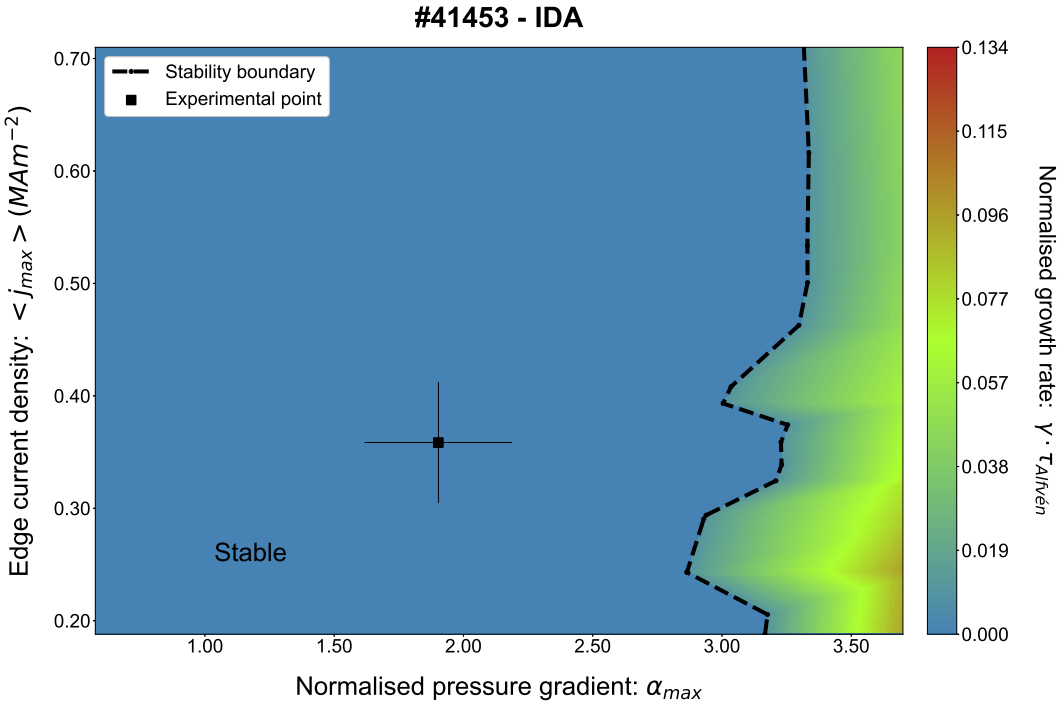

Figure 4.11: Stability diagram showing the position of the operational point (with errorbars) with respect to the stability boundary for #41453 in the time interval 6.45 - 6.75 s using IDA as source.

Note that the stability boundary in graph 4.10 is represented with a scatter plot as the dashed line did not delimit well.

Time interval: 7.10 - 7.40 s

The stability diagram for #41453 in the time interval 7.10 - 7.40 s is displayed in graph 4.12 for AUGPED (IDA is not taken into consideration since no good points were available).

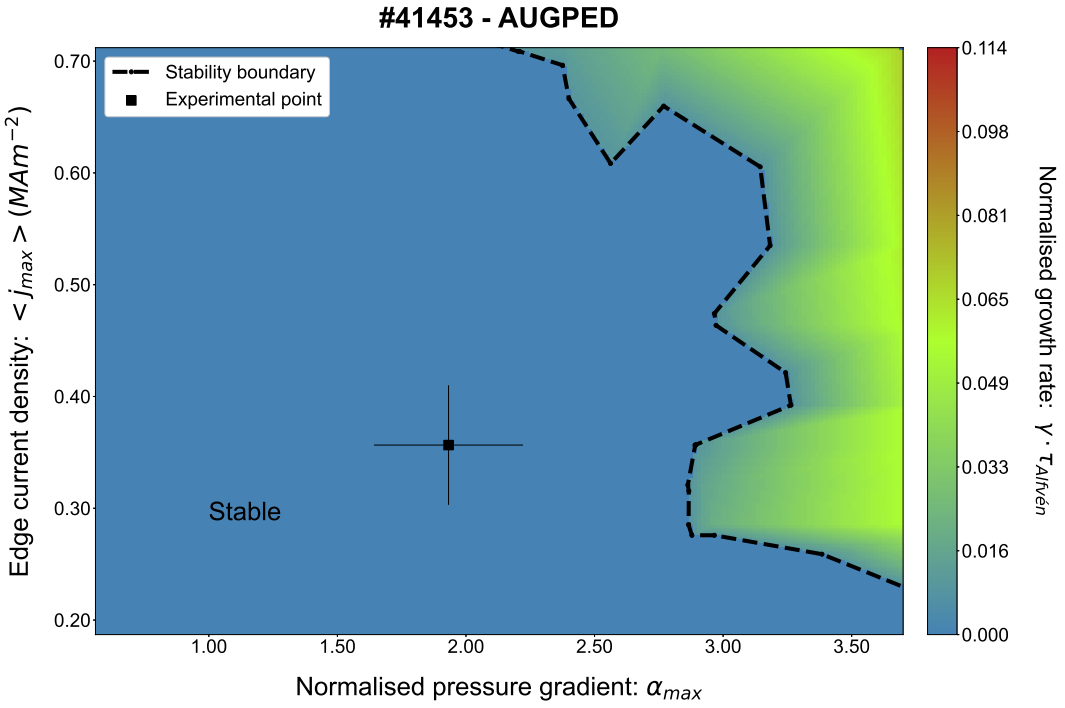

Figure 4.12: Stability diagram showing the position of the operational point (with errorbars) with respect to the stability boundary for #41453 in the time interval 7.10 - 7.40 s using AUGPED as source.

Discharge #41454

A list of the main parameters related to #41454 is shown in table 4.8:

	B_ϕ (T)	I_p (MA)	n_e ($\times 10^{19}$ m^{-3})	q_{95}	P_{heat} (MW)	κ	δ_{upper}	δ_{lower}
#39429	-2.5	0.8	7.9	5.3	NBI: 9.8 EC: 1.2	1.68	0.24	0.45

Table 4.8: Main parameters for #41454.

The triangularity is a high δ.

The *flattop* phase here is 3.16 - 7.39 s.

Three different time intervals have been taken into account for #41454, reported in the following subsections.

Time interval: 5.85 - 6.10 s

The pedestal stability diagram for #41454 in the time interval 5.85 - 6.10 s is displayed in graph 4.13 for AUGPED (IDA is not taken into consideration since no good points were available).

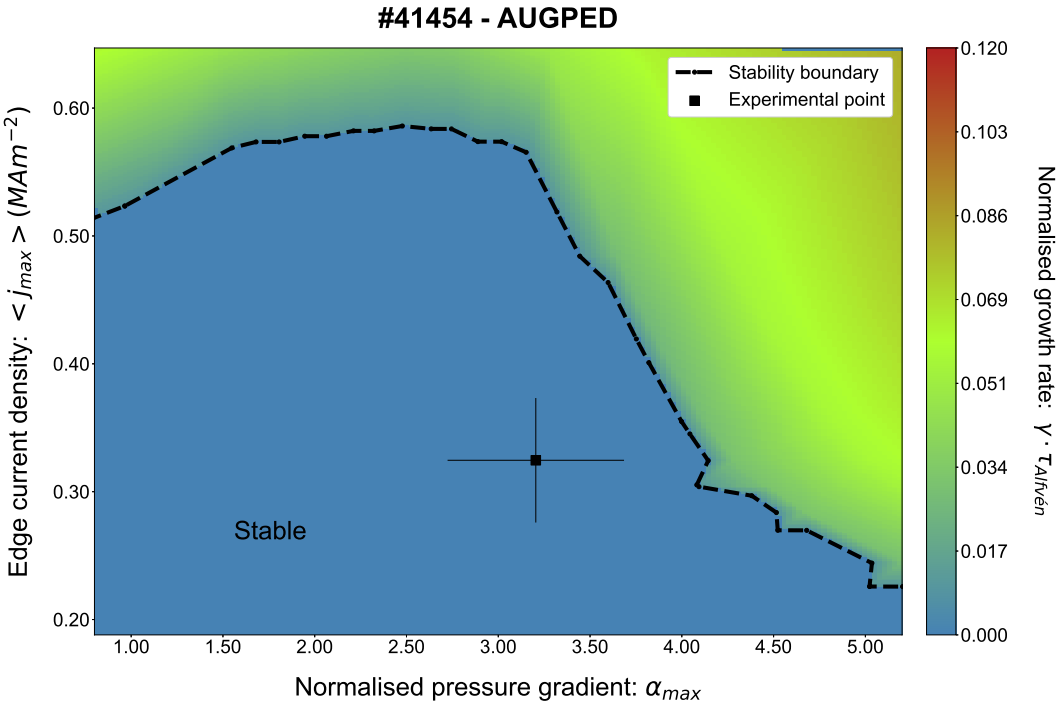

Figure 4.13: Stability diagram showing the position of the operational point (with errorbars) with respect to the stability boundary for #41454 in the time interval 5.85 - 6.10 s using AUGPED as source.

Also here, starting with AUGPED, the experimental point is within the boundary.

Time interval: 6.15 - 6.40 s

The pedestal stability diagram for #41454 in the time interval 6.15 - 6.40 s is displayed in graph 4.14 for AUGPED (IDA is not taken into consideration since no good points were available).

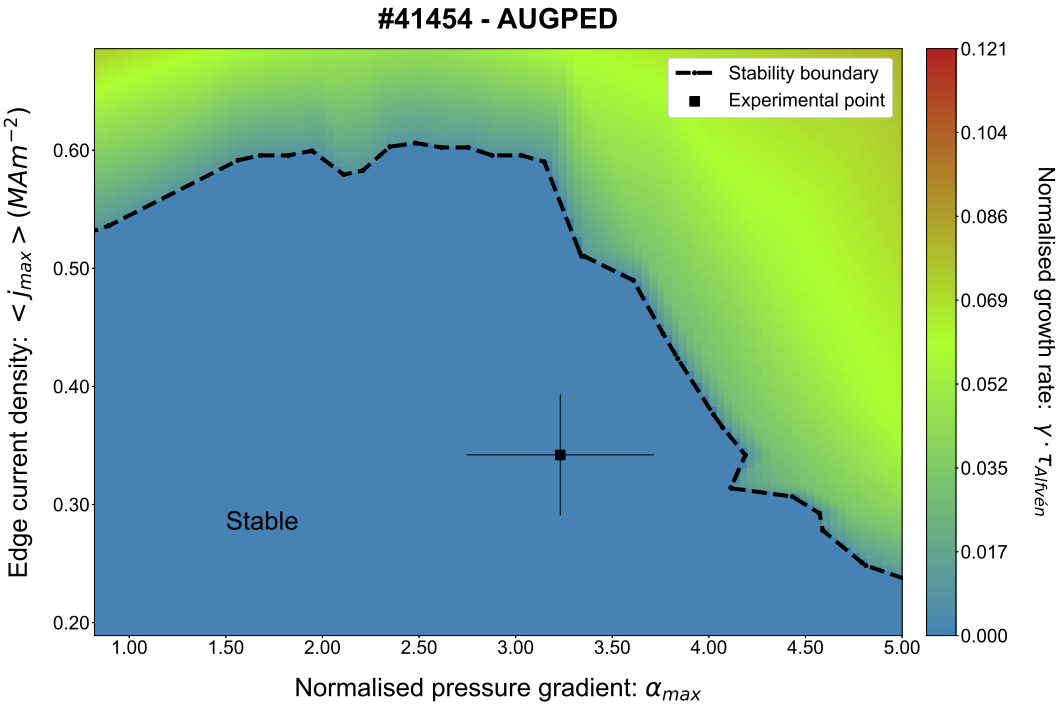

Figure 4.14: Stability diagram showing the position of the operational point (with errorbars) with respect to the stability boundary for #41454 in the time interval 6.15 - 6.40 s using AUGPED as source.

4.5.1 Discussion on He plasma

As far as the study of the helium plasma is concerned, the point almost always turns out to be inside the boundary, thus being stable. If the pedestal is ideal PB limited, the point should lie on the stability boundary. This does not happen in the cases studied, which implies that the pedestal is not PB limited. Possible causes can be attributed to the resistivity of the plasma.
Furthermore, ELMs are much more frequent with helium plasmas than with hydrogen plasmas.

Chapter 5

Conclusions

The aim of the current thesis work, carried out at Max-Planck-Institut für Plasmaphysik (IPP) in Garching (Germany), is the study of magnetohydrodynamic stability analysis of the pedestal in plasmas with different main ions, deuterium and helium, in the ASDEX Upgrade tokamak.

The theory of magnetohydrodynamics (MHD), as presented in detail in the second chapter, describes the plasma, through macroscopic quantities, as a combination of charged fluids. MHD combines electromagnetic and hydrodynamic description of the plasma in order to obtain a comprehensive picture of both static states and dynamic processes. This theory is essential in the study of the edge localised modes (ELMs), quasi-periodic explosive instabilities at the plasma edge which expel particles and energy on ms time-scales due to periodic relaxations of the edge transport barrier in high-confinement mode (H-mode).

In detail, the H-mode dramatically improves the confinement properties of present tokamak plasmas, it is therefore the scenario envisioned for future fusion reactors. Its main characteristic is the formation of a pedestal, a zone of steep temperature and density gradients at the edge of the plasma, by means of a transport barrier, which is limited in height by the onset of edge localized modes.

While ELMs in today's machines are safe, it is expected that they may significantly harm the machine's components when scaled up to a fusion reactor device. As a result, there is significant interest in understanding and exploiting alternative regimes with high confinement mode but without ELMs.

After selecting the stationary phase of several parameters of the plasma to be examined such as fuelling rates, density, temperature, heating power, stored energy (see graph 4.1), the process involves profile fitting tools with two different approaches:

- IDA, a Bayesian probability-based computational method;
- AUGPED, a manual fitting tool in which a modified hyperbolic tangent function for the pedestal area is employed.

The profile fittings are starting elements for the stability analysis.

The stability analysis of the pedestal is then carried out by the automation of a workflow which runs codes to test the pedestal MHD stability, such as MISHKA, starting from a standardized set of experimental information and with the use of the HELENA to calculate the Grad-Shafranov equation for a toroidal axisymmetric plasma. From MISHKA the growth rates normalised with the Alfvén timescale $\tau_{Alfvén}$ are obtained which help to interpret the plasma stability.

The workflow is applied to a database of experimental data from the ASDEX Upgrade tokamak to study the properties of the pedestal.
It is particularly important to provide a rough estimate of the distance to the MHD stability boundary in the various ELM-free regimes to understand how robust these regimes are and the margin a given regime has before a large ELM is triggered.
The study is performed by means of stability diagrams, which are contour plots (2D surface plots) dependent on the pressure normalised gradient α_{max}, the edge current density $< j_{max} >$ and the normalised growth rate $\gamma \cdot \tau_{Alfvén}$.

The main results of this thesis work for D and He plasmas follow:

- For deuterium plasmas, through AUGPED source, operational point positions on the stability boundary, within the limits of the uncertainty given at 15%, are obtained, as expected.
  If the pedestal is ideal Peeling-Ballooning (PB) limited, the point should lie on the stability boundary. The uncertainty is rough, but reasonable considering the uncertainty on radial resolution, temporal resolution, the diagnostic measurement, the source used to the fittings and the gradient measurement;

- For helium plasmas, on the other hand, it can be seen that the points are within the stability boundary, in the stable part of the plasma, this may be attributable to the influence of plasma resistivity. The pedestal, in these cases, is not PB limited.
  Furthermore, ELMs are much more frequent in He plasmas than in H plasmas.

A good example of a stability diagram is encountered in the graph 4.6 for deuterium plasma, where the operational point is with good approximation on the MHD stability boundary.

Bibliography

Books

[1] R.J. Goldston. *Introduction to Plasma Physics*. CRC Press, 2020.
https://books.google.it/books?id=7kM7yEFUGnAC.

[2] F. Chen. *Introduction to Plasma Physics and Controlled Fusion*. Springer (3rd edition), 2016.
https://doi.org/10.1007/978-3-319-22309-4

[3] J. Wesson and D. J. Campbell, *Tokamaks*. International Series of Monographs on Physics. OUP Oxford, 2011.
https://books.google.it/books?id=XJssMXjHUr0C

[4] A. R. Choudhuri. *The Physics of Fluids and Plasmas. An Introduction for Astrophysicists*. Cambridge University Press, 1998.
https://doi.org/10.1017/CBO9781139171069

[5] L. J. Reinders. *The Fairy Tale of Nuclear Fusion*. Springer International Publishing AG, 2021.
https://doi.org/10.1007/978-3-030-64344-7.

[6] K. Miyamoto. *Plasma Physics and Controlled Nuclear Fusion*. Springer, 2005.
https://doi.org/10.1007/3-540-28097-9

[7] H. Zohm. *Magnetohydrodynamic Stability of Tokamaks*. WILEY-VCH Verlag GmbH & Co. KGaA, 2015.
https://doi.org/10.1002/9783527677375

[8] J. Freidberg. *Ideal MHD*. Cambridge University Press, 2014.
https://doi.org/10.1017/CBO9780511795046

Articles

[9] C. Horowitz. *Paris Agreement*. International Legal Materials, 55(4), 740-755, 2016.
https://doi.org/10.1017/S0020782900004253

[10] A. Bradshaw. T. Hamacher, and U. Fischer, *Is nuclear fusion a sustainable energy form?* Fusion Engineering and Design, vol. 86, no. 9, pp. 2770–2773, 2011.
https://doi.org/10.1016/j.fusengdes.2010.11.040

[11] B. Bigot. *Progress toward ITER's First Plasma*. Nucl. Fusion 59 112001, 2019.
https://doi.org/10.1088/1741-4326/ab0f84

[12] T. Odstrcil. *On the Origin, Properties, and Implications of Asymmetries in the Tungsten Impurity Density in Tokamak Plasmas*. 2017.
https://doi.org/10.13140/RG.2.2.22204.39040

[13] A. L. Manini. *Analysis and interpretation of the plasma dynamic response to additional heating power using different diagnostics*. EPFL, 2002.
https://infoscience.epfl.ch/record/33075

[14] T. Luda di Cortemiglia. *Integrated modeling of tokamak plasma confinement combining core and edge pedestal physics. PhD thesis*, 2020.
https://pure.mpg.de/rest/items/item_3283708/component/file_3283711/content

[15] M. G. Dunne. *Inter-ELM evolution of the edge current density profile on the ASDEX upgrade tokamak. PhD thesis*, 2013.
https://cora.ucc.ie/items/7de5b7e5-fea7-425b-a820-157b97a3f4a8

[16] E. Wolfrum, F. Aumayr, D. Wutte *et al.*. *Fast lithium-beam spectroscopy of tokamak edge plasmas. Review of Scientific Instruments.* 64(8):2285, 1993.
https://doi.org/10.1063/1.1144460

[17] O. Gehre. *The HCN-laser-interferometer of the divertor tokamak ASDEX. International Journal of Infrared and Millimeter Waves.* 5(3):369 – 379, 1984.
https://doi.org/10.1007/BF01009664

[18] N. A. Salmon . *First electron temperature edge measurements on the asdex upgrade tokamak using a heterodyne radiometer.* International Journal of Infrared and Millimeter Waves (15), 53 – 60, 1994.
https://cora.ucc.ie/items/7de5b7e5-fea7-425b-a820-157b97a3f4a8

[19] G. F. Harrer, *On the origin and transport of small ELMs. PhD thesis*, 2020.
https://doi.org/10.34726/hss.2020.44863

[20] J. W. Coenen, *The Influence of the Dynamic Ergodic Divertor on the Radial Electric Field at the Tokamak TEXTOR*, 2009.
https://www.osti.gov/etdeweb/biblio/21226814

[21] J. Puchmayr, *Optimization of Pedestal Stability on ASDEX Upgrade. Master's thesis*, 2020.
https://pure.mpg.de/rest/items/item_3262339/component/file_3262340/content

[22] L. Radovanovic, *Ballooning stability analysis of the ASDEX-Upgrade small-ELM regime. Master's thesis*, 2020.
https://doi.org/10.34726/hss.2020.71723

[23] C. P. Perez, *et al.* . *Washboard modes as ELM-related events in JET*, 2003.
https://doi.org/10.1088/0741-3335/46/1/005

[24] A. Dinklage, *et al.* . *Integrated Data Analysis for Fusion: A Bayesian Tutorial for Fusion Diagnosticians.* AIP Conf. Proc. 988, 471–480, 2008.
https://doi.org/10.1063/1.2905117

[25] R. Fischer, C. J. Fuchs, B. Kurzan, W. Suttrop, E. Wolfrum and ASDEX Upgrade Team, *Integrated data analysis of profile diagnostics at Asdex upgrade.* Fusion Science and Technology, 2010.
https://doi.org/10.13182/FST10-110

[26] R.J. Groebner, *et al.* . *Progress in quantifying the edge physics of the H mode regime in DIII-D.* Nuclear Fusion 41 1789, 2001.
https://doi.org/10.1088/0029-5515/41/12/306

[27] D. P. Boyle, *et al.* . *The relationships between edge localized modes suppression, pedestal profiles and lithium wall coatings in NSTX.* Plasma Phys. Control. Fusion 53 105011, 2011 .
https://doi.org/10.1088/0741-3335/53/10/105011

[28] R. Zille C. Konz, *HELENA Fixed Boundary Equilibrium Solver*, 2007.

[29] G.T.A. Hujismans, J. P. Goedbloed and W. Kerner. *Isoparametric bicubic hermite elements for solution of the Grad-Shafranov equation.* International Journal of Modern Physics C, 2(1):371–376, 1991.
https://doi.org/10.1142/S0129183191000512

[30] A. B. Mikhailovskii, G. T. A. Huysmans, W. O. K. Kerner and S. E. Sharapov. *Optimization of computational MHD normal-mode analysis for tokamaks.* Plasma Phys. Rep. 23 844–57, 1997.
https://doi.org/10.1134/1.952514

[31] R. L. Miller, M. S. Chu, J. M. Greene, *et al. Toroidal coupling of ideal magnetohydrodynamic instabilities in tokamak plasmas.* Phys. Plasmas, 5(4), 973, 1998.

[32] P. A. Schneider, *et al. The dependence of confinement on the isotope mass in the core and the edge of AUG and JET-ILW H-mode plasmas.* Nucl. Fusion 62, 2021.
https://doi.org/10.1088/1741-4326/ac3e82

[33] I. Pusztai, J. Candy and P. Gohil. *et al. Isotope mass and charge effects in tokamak plasmas.* Phys. Plasmas 18, 122501, 2011.
https://doi.org/10.1063/1.3663844

[34] T. C. Luce. *An analytic functional form for characterization and generation of axisymmetric plasma boundaries.* Plasma Phys. Control. Fusion 55 095009, 2013.
https://doi.org/10.1088/0741-3335/55/9/095009

[35] T. H. Osborne, *et al. The effect of plasma shape on H-mode pedestal characteristics on DIII-D.* Plasma Phys. Control. Fusion 42 A175, 2000.
https://doi.org/10.1088/0741-3335/42/5A/319

[36] T. Luda, *et al. Integrated modeling of ASDEX Upgrade plasmas combining core, pedestal and scrape-off layer physics.* Nucl. Fusion 60 036023, 2020.
https://doi.org/10.1088/1741-4326/ab6c77

[37] L. Frassinetti, *et al. Role of the separatrix density in the pedestal performance in deuterium low triangularity JET-ILW plasmas and comparison with JET-C.* Nucl. Fusion 61 126054, 2021.
https://doi.org/10.1088/1741-4326/ac3363

[38] M G Dunne, *et al. The role of the density profile in the ASDEX-Upgrade pedestal structure.* Plasma Phys. Control. Fusion 59 014017, 2017.
https://doi.org/10.1088/0741-3335/59/1/014017

[39] F. Troyon, *et al. MHD-Limits to Plasma Confinement.* Plasma Phys. Control. Fusion 26 209, 1984.
https://doi.org/10.1088/0741-3335/26/1A/319

[40] A. Hakola, *et al. Helium plasma operations on ASDEX Upgrade and JET in support of the non-nuclear phases of ITER.* 29th Fusion Energy Conference, 2023.
https://conferences.iaea.org/event/316/contributions/27811/

Websites

[41] Max-Planck Institute for Plasma Physics (IPP).
https://www.ipp.mpg.de/en

[42] H. Ritchie, M. Roser and P. Rosado. *Energy.* Our World In Data.
https://ourworldindata.org/energy

[43] H. Ritchie, M. Roser and P. Rosado. *CO_2 and Greenhouse Gas Emissions.* Our World In Data.
https://ourworldindata.org/co2-and-greenhouse-gas-emissions

[44] https://terpconnect.umd.edu/~wbreslyn/chemistry/isotopes/isotopes-notation.html

[45] ITER. Advantages of Fusion.
https://www.iter.org/sci/Fusion

[46] M. Barbarino. *What is Nuclear Fusion.* IAEA, 2022.
https://www.iaea.org/newscenter/news/what-is-nuclear-fusion

[47] F. Fleschner, M. Roser and P. Rosado. *The next Step for ASDEX Upgrade*. EUROfusion, 2022. https://euro-fusion.org/member-news/the-next-step-for-asdex-upgrade/

[48] Helium. Britannica. https://www.britannica.com/science/helium-chemical-element

[49] Deuterium. Britannica. https://www.britannica.com/science/deuterium

[50] EUROfusion Glossary. https://euro-fusion.org/services/eurofusion-glossary/